2007-03-26

In vivo monitoring of collagen-sponge remodeling using MRI

Sivakumar P. Kandasamy
Worcester Polytechnic Institute

In vivo monitoring of collagen-sponge remodeling using MRI

A thesis submitted to the faculty of the
WORCESTER POLYTECHNIC INSTITUTE
in partial fulfillment of the requirements for the
degree of Master of Science
in Biomedical Engineering

by

Sivakumar P Kandasamy

March 2007

Approved by

Christopher H. Sotak Ph.D.
Professor and Head, Major Advisor
Biomedical Engineering Department
Worcester Polytechnic Institute

George Pins Ph.D.
Associate Professor
Biomedical Engineering Department
Worcester Polytechnic Institute

Glenn Gaudette Ph.D.
Assistant Professor
Biomedical Engineering Department
Worcester Polytechnic Institute

ACKNOWLEDGEMENTS

I would like to thank my advisor, Chris Sotak for giving me the opportunity to work with him. I would like to thank him for helping me to grow and expand my knowledge as graduate student in the MRI field. His fascinating personality, rigorous knowledge in the MRI field and his achievements make him a living role model for me.

I would also like to thank George Pins, for his collaboration on the biomaterial studies. His friendly nature and good understanding with me, made it comfortable to work with him in his lab. I admire his commitment and his wonderful, insightful comments made my time fun.

Glenn Gaudette has been a great source of guidance and suggestions and has greatly helped to improve my work as a member of my thesis committee.

Many thanks to my friend and co-project mate, Stuart Howes for his help in each and every aspect of my thesis. His wholehearted support has made my time with him unforgettable.

I would like to forward my special thanks to Lisa Wall for her dedicated assistance in my lab work. Thanks to Deborah Bordage and Jean T. Siequist for the utmost support in office work.

I appreciate the cooperation and assistance of my MRI lab mates, Dave Bennett, Govind Bhagavatheeswaran, James Bouley, and Erica Henning for their support in all phases of my lab work.

My brother Kumarasamy Kandasamy and his family, my parents, my sisters and all my friends deserve thanks for their love and support.

And last but not least, I would like to thank the WPI administration and community for accepting me as one among them and providing a wonderful environment in which to learn a new dimension of science.

Table of Contents

Abstract

The evaluation of the remodeling of soft biomaterial implants often involves surgical removal of the implant for subsequent histological assessment. This approach is very resource intensive, often destructive, and imposes practical limitations on how effectively these materials can be evaluated. Magnetic resonance imaging (MRI) has the potential to non-invasively monitor the remodeling of collagen sponges, specifically the biodegradation, cellular infiltration, extracellular matrix deposition and angiogenesis within the sponge. This project involves the development of an *in vivo* model system for the evaluation of collagen-sponge remodeling using MRI and conventional histological techniques. Collagen sponges made using insoluble bovine collagen, and subjected various crosslinking treatments, were implanted subcutaneously into rats. Changes in water T_2 relaxations times, water apparent diffusion coefficients (ADC), and MRI contrast agent uptake/washout were collected using spin-echo and diffusion-weighted MRI pulse sequences. These measurements were compared with histological assessments of sponge remodeling. Regions of differential cellularity were distinguished using calculated T_2 maps and confirmed by histology. Calculated ADC maps corroborated these results and showed a decreasing trend with increased tissue in-growth. Results from MRI-contrast-agent studies were consistent with the development of angiogenesis within the sponge over time. The MRI approach allows for longitudinal studies that significantly reduce the resources required to evaluate these materials as well as improves the quality of the statistical information obtained from these studies.

1. Nuclear Magnetic Resonance – An Introduction

This chapter addresses the principles of nuclear magnetic resonance (NMR) and terminology used in this thesis. The chapter was written based on the information from Dowdey *et al*.[1], Marinus *et al.* [2], Morris [3], Harris [4], Farrar and Becker [5], Gadian [6], Tofts [7], King *et al.* [8], and Salibi and Brown [9].

1.1 Basic Physics

1.1.1 Magnetic Dipole Moment

The electrons of each atom orbit around the nucleus and the nucleus rotates on its axis. This spinning nucleus results in the orbital motion of the nucleon (protons and neutrons) around the center of the nucleus, thus each nucleon has angular momentum associated with it. At the lowest energy state, a pair of protons (or neutrons) in same energy level precess in opposite directions (i.e., referred to as spin-up and spin-down) effectively canceling each other out in terms of net spin. So, under the lowest-energy conditions, the angular momentum of unpaired protons (or neutrons) is equal to the net nuclear angular momentum.

Protons rotating around the nuclear center can be thought of as a sphere of positive charge flow with a small magnetic field aligned along the axis of rotation. This magnetic field is analogous to a current flowing through a loop of wire, with the resulting magnetic induction occurring perpendicular to the plane of the loop. This nuclear magnetic field is referred to as the Magnetic Dipole Moment (MDM).

In the classical description, the nuclear magnetic dipole moment, $\boldsymbol{\mu}$, is represented as:

$$\boldsymbol{\mu} = (e/2m_p)\,\mathbf{P} \qquad (1.1)$$

(e – charge of a proton; m_p – mass of a proton; **P** – proton spin angular momentum)

In general, the nuclear magnetic moment may be expressed in terms of the gyromagnetic ratio (γ),

$$\boldsymbol{\mu} = \gamma \mathbf{P} \qquad (1.2)$$

which is proportional to the charge-to-mass ratio of the nucleus and thus is unique for each NMR-visible nucleus or isotope.

1.1.2 Spin Angular Momentum

The nucleons orbiting about the center of the nucleus create spin angular momentum, which is related to the nuclear spin quantum number I. The net value for I is determined by number of unpaired nucleons. For example, the ^{1}H isotope has one unpaired proton and thus I = 1/2. The possible spin orientations of the ^{1}H nucleus are shown in Figure 1-1

The magnitude of the spin angular momentum is given by

$$|P| = \hbar [I(I+1)]^{1/2}, \qquad (1.3)$$

where $\hbar = h/2\pi$ and h = Plank's constant. For ^{1}H, the spin angular momentum is: $|P| = \sqrt{2}\,\hbar$.

The external magnetic field, B_o, is defined as being aligned along the z axis of a Cartesian coordinate frame of reference. If the vector **P** is allowed to point in the same direction, then the projection of **P** onto the z axis is given by,

$$P_z = \hbar m_I \qquad (1.4)$$

where m_I is directional or magnetic spin quantum number and its possible values are -I, -I+1, …, I-1, +I. For a spin-1/2 nucleus: $m_I = +1/2$ and $-1/2$; $P_z = \pm \hbar/2$; and $|P| = (\sqrt{3}/2)\,\hbar$. Thus, the angle, θ, between the two possible orientations of the vector P is 54°44'.

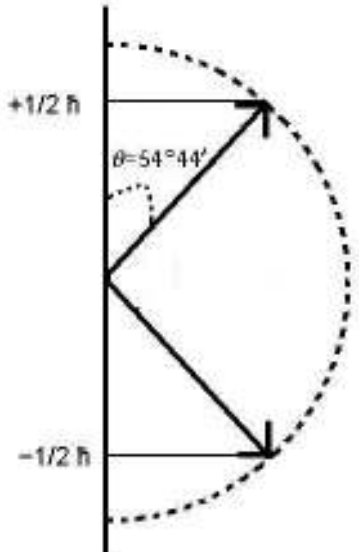

Figure 1-1. Orientation of Spin Angular Momentum Vector P for a Spin-1/2 Nucleus (e.g., ^{1}H).

1.2 Magnetic Resonance

1.2.1 Energy States

The ^{1}H nucleus, with I = 1/2, exhibits two possible orientations when placed in an external magnetic field B_o (referred to as spin-up and spin-down). The spin-up orientation, parallel to B_o, occupies a lower energy state. The spin-down orientation, anti-parallel to B_o, exists in a higher energy state.

The potential energy that arises when a proton is placed in an external magnetic field is given by,

$$E = -\mu_z B_o \qquad (1.5)$$

$\mu_z = \gamma m_I \hbar$; $m_I = -I, -I+1, \ldots, I-1, I$ (where $m_I = +1/2$ and $-1/2$ for I = 1/2)

So, for the spin-down orientation,

$E_2 = \gamma \hbar B_o/2$ (Since $m_I = -1/2$ for the higher energy state) (1.6)

and, for the spin-up orientation,

$$E_1 = - \gamma \hbar B_o/2 \qquad \text{(Since } m_I = +1/2 \text{ for the lower energy state)} \quad (1.7)$$

and the energy difference between these two states is given by

$$\Delta E = E_2 - E_1 = \gamma \hbar B_o \qquad (1.8)$$

1.2.2 Boltzmann Distribution

In practice, the NMR experiment detects only the population difference between two energy states which are populated a large number of nuclear spins simultaneously. According to the Boltzmann distribution, for spin-1/2 nuclei, the population ratio between higher energy state and lower energy state is,

$$N_{E2}/N_{E1} = e^{-\Delta E/kT} \qquad (1.9)$$

where k = Boltzmann constant = 1.38×10^{-23} J K^{-1}, T = Temperature (absolute).

This ratio is unique for a given nucleus and magnitude of B_o. The net sum of all of the individual nuclear magnetic moments (effectively the population difference between the two energy states), M_o, is measured as NMR signal.

1.2.3 Larmor Frequency

From a classical-physics point-of-view, an external magnetic field B_o will exert a torque on the nuclear magnetic moments, causing them to precess about B_o. The Larmor precessional frequency is defined as,

$$\upsilon = \gamma B_o/2\pi \qquad (1.10)$$

For example, in a 2.0 Tesla magnetic field, the Larmor frequency of ^{1}H is 85.557 MHz ($\gamma/2\pi$ = 42.58 MHz/T). Since the gyromagnetic ratio is unique for each nucleus, the Larmor precessional frequency for a particular nucleus is also unique for a given B_o field strength.

Radiofrequency excitation (at a frequency equal to the Larmor frequency) can rotate the net magnetization vector, M_o, from the z-axis into the x-y plane of the Cartesian coordinate system, where it can be measured as the NMR signal.

1.2.4 Free Induction Decay

The NMR experiment can be divided into two phases: excitation and detection. The excitation phase of the experiment is achieved by irradiating the nuclei with a radio frequency (RF) signal transmitted via an RF coil. The geometry of the coil creates a B_1 field (the magnetic field component of the RF) in the transverse (x-y) plane that is orthogonal to the external static field B_o oriented longitudinally along the z-axis. The nuclear magnetization can have two components: one parallel to the B_o direction (M_z) and other orthogonal to B_o (M_{xy}). At the Boltzmann equilibrium, $M_z = M_o$ and the net transverse magnetization (M_{xy}) is zero, because of the random position of the x-y components of the individual nuclear magnetic moments – with respect to each other – as they precess about the B_o field. When a B_1 field is applied at the Larmor frequency, the nuclei absorb energy and M_z is rotated into the x-y plane, creating coherent transverse magnetization (M_{xy}).

According to Faraday's Law, the coherent M_{xy} components of magnetization will induce an electromotive force (EMF) into the RF coil which is subsequently detected as the NMR signal. Following RF excitation, the M_z component of magnetization exponentially returns to the Boltzmann equilibrium value by dissipating energy to the surroundings (or "the lattice"). The other component, M_{xy}, decays to zero exponentially, because of the loss of phase coherence between the individual nuclear magnetic moments precessing in the x-y plane. The resulting Free

Induction Decay (FID) is detected as an exponentially-dampened, sinusoidal signal at the Larmor frequency of the nuclei [1].

1.3 MRI Parameters

1.3.1 Spin-Spin Relaxation Time (T_2)

Immediately following the RF excitation pulse, the M_{xy} magnetization decays exponentially to zero because of B_o-field inhomogeneities and other processes. This transverse relaxation process is given by

$$M_{xy}(t) = M_o \exp [-t / T_2^*], \quad t = \text{time} \qquad (1.11)$$

The characteristic plot of the T_2^* relaxation curve (i.e., Eq. 1.11) is shown in Figure 1-2. The transverse relaxation time constant, T_2^*, gives information about intrinsic properties of the particular sample and may contain contributions from a variety of sources (e.g., the intrinsic spin-spin relaxation time, magnetic field inhomogeneities and susceptibility effects, and molecular diffusion) and is expressed as

$$1/T_2^* = 1/T_{2\ \text{Intrinsic}} + 1/T_{2\ \text{Inhomogenity}} + 1/T_{2\ \text{Susceptibility}} + 1/T_{2\ \text{Diffusion}} + \ldots \qquad (1.12)$$

The T_2^* time constant is the time required for the M_{xy} to decrease to 36.8% of the original value following the RF pulse.

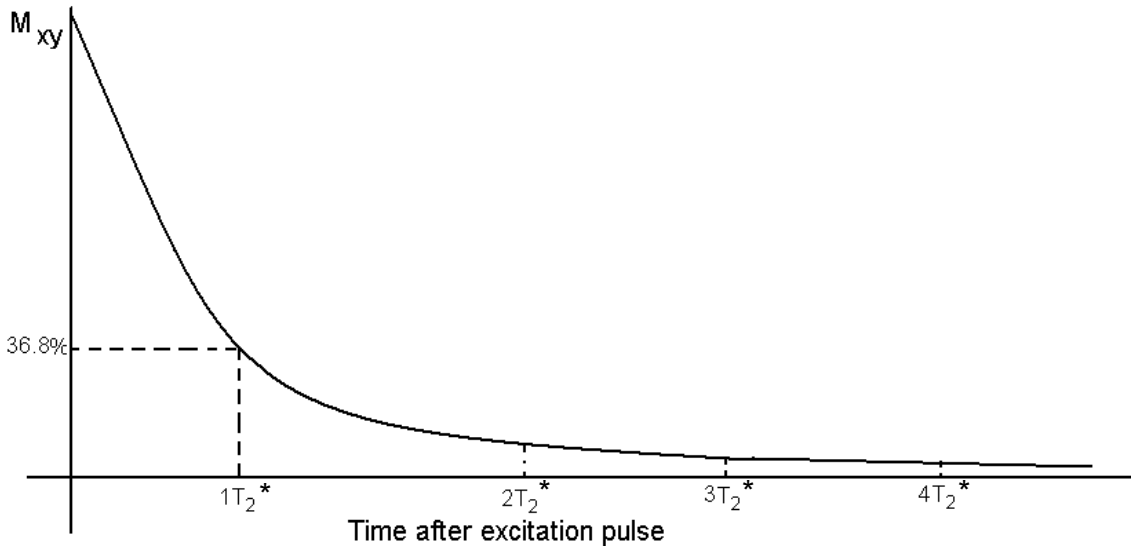

Figure 1-2. T_2^* Decay of Transverse Magnetization, M_{xy}, Following a Radiofequency (RF) Pulse.

The intrinsic T_2 relaxation rate (i.e., $R_{2\ Intrinsic} = 1/T_{2\ Intrinsic;}$ the first term in Eq. 1.11) of water molecules can be expressed in terms of a fast exchange between two water pools – bound and bulk water [10] – as given by:

$$1/T_{2(OBSERVED)} = f\,(1/T_{2(BOUND)}) + (1 - f)\,(1/T_{2(BULK)}), \qquad (1.13)\ [11]$$

where f is the fractional contributions from each pool.

The bulk-water pool represents free water in the bulk phase where there is little interaction between the water molecules and the biological milieu. In this case, water molecules exhibit relatively fast molecular motions. The bound water pool represents water molecules that are hydrogen-bonded directly to macromolecules (proteins) or cellular constituents (e.g., cell membranes, organelles, etc.). In this case, the molecular motions of the attached water molecules are determined by macromolecular or cellular motions and thus are much slower than for water in the bulk phase.

Figure 1-3 shows a schematic diagram of water in the different motional regimes [12]. Consequently, the presence of macromolecules and cells cause a reduction in the average

rotational frequency of the surrounding water molecules which in turn shortens the measured T_2 value [10, 12, 13]. The T_2 relaxation time associated with the bulk-water fraction is normally referred as the 'long T_2' component and that of the bound-water fraction as the 'short T_2' component [14]. Therefore, changes in the relative fractions of bulk and bound water result in changes in the observed T_2 values.

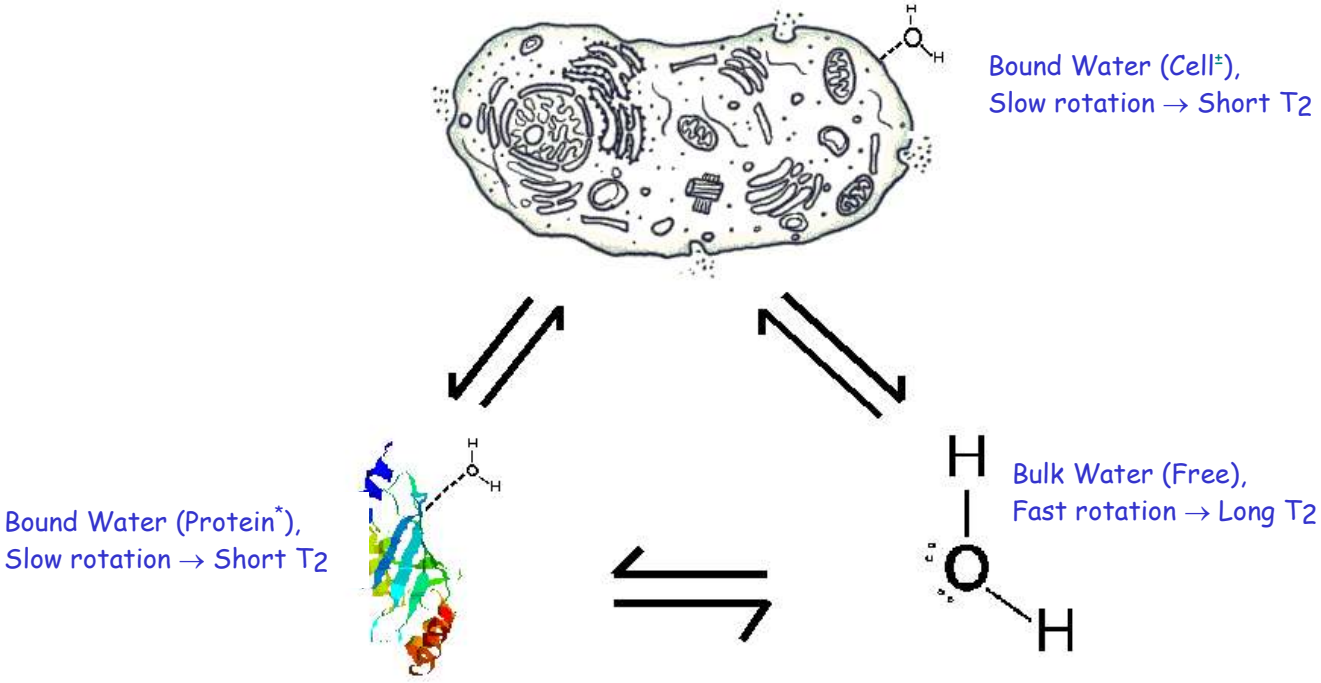

Figure 1-3. Schematic Representation of Bound and Bulk Water Phases and Their Effects on Water T_2 Relaxation Times.

* http://condor.urbb.jussieu.fr/~debrevern/PEELING/in_pdb_anim.gif
± http://www.biology4kids.com/files/art/cell_over1.gif

1.3.2 Spin-Lattice Relaxation Time (T_1)

The application of a RF pulse rotates the longitudinal magnetization, M_z, into the x-y plane. After the RF excitation, M_z relaxes back to the Boltzmann equilibrium by dissipating energy to the lattice. The recovery of M_z as a function of time is given by,

$$M_z(t) = M_o\,[1- \exp(-t / T_1)\,], \quad \text{where } t = \text{time.} \qquad (1.14)$$

The time constant of the exponential recovery is called the T_1 or spin-lattice relaxation time. The characteristic plot of T_1 relaxation curve (Eq. 1.14) is shown in Figure 1-4. The T_1 relaxation time is the time required for M_z to recover to 63% of the Boltzmann equilibrium value after at 90^o rotation from the z-axis into the x-y plane (i.e., a 90^o RF excitation).

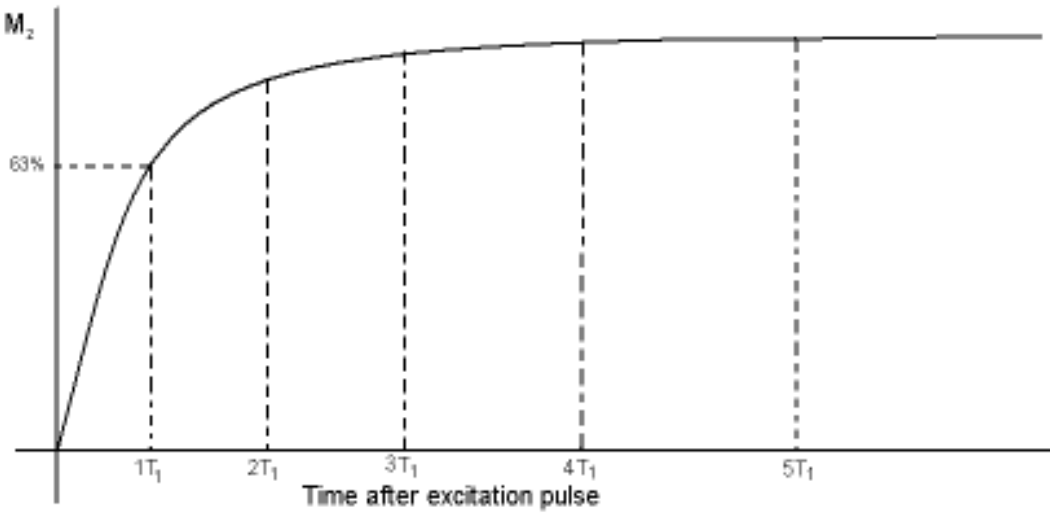

Figure 1-4. T_1 Recovery of the Longitudinal Magnetization, M_z, Following a 90^o Radiofrequency RF Pulse.

1.3.3 Effect of MRI Contrast Agents on T_1 and T_2 Relaxation Times

The T_1 and T_2 relaxation times are affected by many factors such as molecular rotation, molecular translation, molecular collisions, magnetic field inhomogeneities, and the presence of paramagnetic ions (i.e., typically metal ions with unpaired electrons) in the environment. In the presence of paramagnetic ions, the change in T_1 is given by the Bloembergen equation as,

$$\Delta R_1 = \Delta(1/T_1) = 12\ \pi^2\ \gamma_N^2\ E\ \mu^2\ N / 5KT, \qquad (1.15)$$

where ΔR_1 = increase in relaxation over pure solvent, N = number of ions per cm^3 (concentration), μ = magnetic moment of the paramagnetic ion, T = absolute temperature, and γ_N, E, K are physical constants.

So, when a MRI contrast agent is introduced into the tissue environment, it increases the paramagnetic ion concentration in the tissue where the contrast agent resides. The T_1 relaxation time of the tissue water is decreased [15-17], resulting in a signal intensity increase (and thus increased contrast) in T_1-weighted images [18]. The signal intensity change is directly proportional to the concentration of MRI contrast agent in the tissue [19]. The effects of changes in T_1-relaxation time on MRI contrast enhancement are showed in Figure 1-5. The signal intensity increase in a post-contrast T_1-weighted image, as a percentage with respect to that in the pre-contrast image (noted with an arrow in Figure 1-5) is the extent of contrast enhancement. The degree of contrast enhancement in T_1-weighted images is correlated with the permeability of tissue microvessels (capillaries) [20] as well as the extent of vascularization [21].

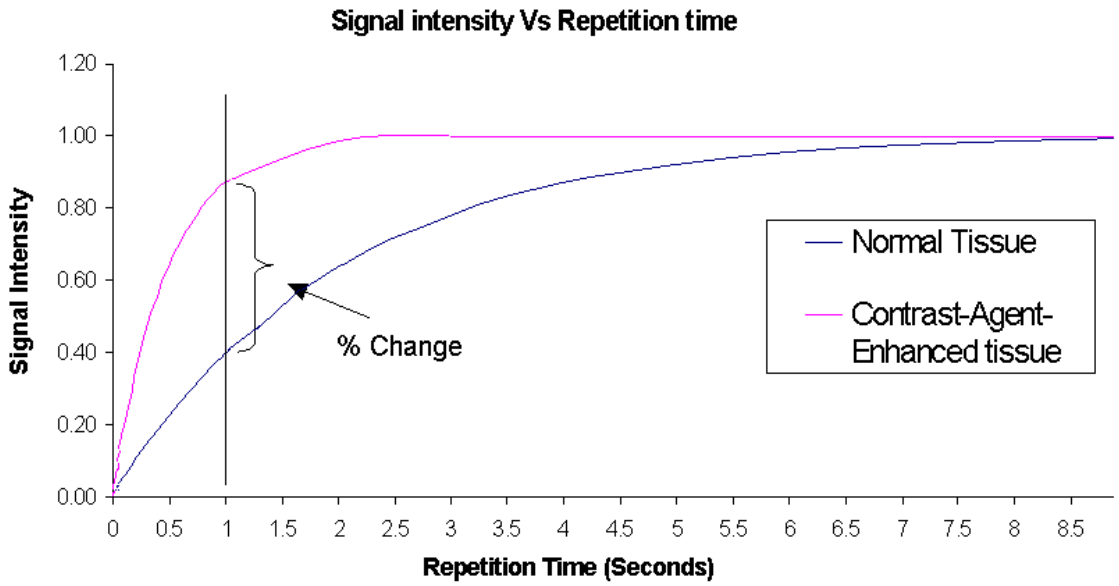

Figure 1-5. T_1 Relaxation Curves for Normal Tissue (blue line) and Tissue Exposed to an MRI Contrast Agent (red line). The Signal-Intensity Difference, as a Percentage at a Given Repetition Time, Translates into MRI Contrast Differences Under Those Conditions.

1.4 Imaging Techniques

1.4.1 Gradient Coils and k-Space

The fundamental basis of MRI is to vary the B_o such that each voxel in a 2D image experiences a B_o field that is unique to that particular position in space. Three gradient coils, orthogonal to each other, are used to superimpose linear magnetic field gradients on the B_o field. These gradient coils allow spatial encoding in three dimensions, crucial to the basic implementation of the MRI method. These gradients also allow MRIs to be sensitized to translational molecular motion and thus facilitate diffusion imaging. In presence of a linear magnetic field gradient, the Larmor frequency of water in each voxel is given by,

$$\upsilon(d) = \gamma/2\pi \, [B_o + d\, G] \qquad (1.16)$$

where d = spatial position of the voxel along the applied gradient axis and G = applied gradient strength (gauss/cm). So, the superposition of this gradient field on B_o establishes a spatial distribution of frequencies that reflect the spatial positions of the water molecules along the direction of the applied gradient field. During imaging, a composite time-domain signal of oscillating voltage changes is measured, via the RF coil, and then stored in a k-vector within 2-dimensional k-space. The signal collection time (t`) and k-space location is given by,

$$k_x(t`) = {}_o\int^{t`} (\gamma/2\pi)\, G_x(t)\, dt,$$

$$k_y(t`) = {}_o\int^{t`} (\gamma/2\pi)\, G_y(t)\, dt, \qquad (1.17)$$

where $G_x(t)$ and $G_y(t)$ = gradient strength function of time and t = gradient duration. Frequency encoding is performed in the k_x direction by incrementing k for each G_x (or frequency-encoding gradient event) and phase encoding is performed in the k_y direction by increasing G_y or the phase-encoding gradient event. The phase angle acquired by a nuclear spin is given by,

$$\theta = (\gamma/2\pi)\, y \int_{o}^{t} G_y(t)\, dt \qquad (1.18)$$

where y is the position of nuclei along the phase-encoding gradient axis. Two-dimensional Fourier transformation is then used to translate the composite time-domain signals in k-space into the corresponding frequency-domain components that comprise spin-density images [22].

1.4.2 Water Apparent Diffusion Coefficient (ADC)

As was discussed earlier, molecular diffusion also affects the transverse relaxation time. Brownian motion of water molecules can significantly affect the decay of transverse magnetization. The diffusion of water molecules in the bulk phase depends on the temperature of the medium, which in turn affects the extent of the molecular motions and their interactions. In biological systems, however, the diffusion of water molecules is affected by various properties of the environment, such as cellularity, integrity of cellular membranes, cell membrane permeability, cell sizes, cell density, extracellular volume, the presence of extracellular materials and other structural anisotropies [23-25]. In general, the presence of cells and cell membranes decrease water diffusion because they impose barriers/restrictions to molecular translation [26].

Furthermore, the extent of molecular displacement is directly proportional to the time allowed for the molecules to diffuse as well as the diffusion coefficient of the molecules. Consequently, it is usually not possible to measure the actual diffusion coefficient of water in biological systems because of the presence of barriers to free diffusion. However, it is possible to measure an apparent diffusion coefficient (ADC) of water by inserting a pair of diffusion-sensitive gradient pulses into a conventional MRI pulse sequence. In this case, the signal intensity of the received MRI signal then becomes proportional to the degree of molecular

displacement of the water molecules in the sample. The ADC of water molecules *in vivo* can then be calculated from a series of diffusion-weighted MR images [27]. The measured ADC values reflect the degree of restriction experienced by water molecules diffusing inside a tissue or a cellular compartment in a single voxel.

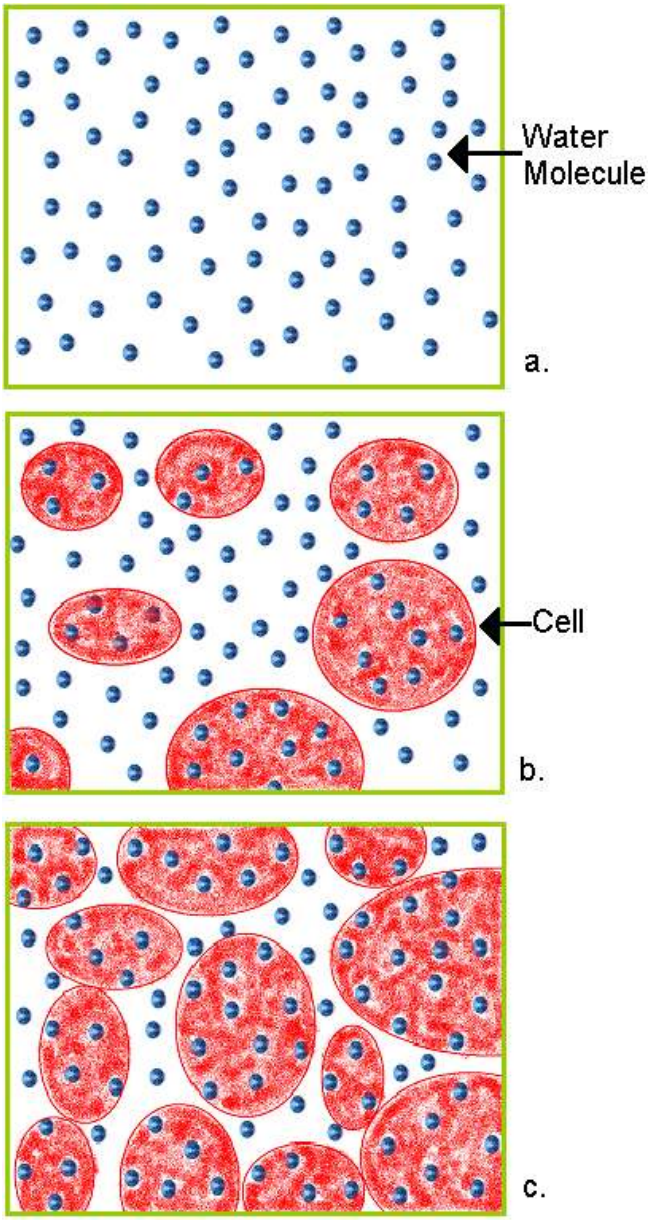

Figure 1-6. **Schematic Diagram Showing the Effects of in vivo Biomaterial Remodeling on the Apparent Diffusion Coefficient (ADC) of Water. a) Initial Condition: No Cells/Large Proteins Present, Unrestricted Movement of Water Molecules, Results in Higher ADC Values; b) Intermediate Condition: Presence of Cells (Cell Membranes) Impose Barriers to Water Diffusion Resulting in Intermediate ADC Values; c) Populated Condition: Dense Cells/Large Proteins Present, Impose More Barriers to Water Diffusion and Result in Lower ADC Values.**

Figure 1-6 shows various scenarios for water molecules diffusing within implanted biomaterials and their effect on the measured ADC values. Generally, ADC values decrease with increasing cellularity [28] as well as the presence of larger protein molecules.

Under *in vivo* conditions, the water ADC can also be dependent on the spatial orientation of the sample with respect to the applied diffusion-gradient direction (i.e., anisotropic). To eliminate this potential orientation dependence, the ADC values are measured along each of the three applied gradient directions (x, y and z) and the average value is calculated.

Diffusion-weighted imaging (DWI) is accomplished by applying pair of diffusion gradients at a particular amplitude (G) for a given duration (δ) separated by a specified time interval (Δ). For a series of DWIs acquired with varying values of G, the water ADC can be calculated from:

$$ADC = [1 / \gamma^2 G^2 \delta^2 t_{diff.}] \cdot \ln [M/M_o], \qquad (1.19)$$

where $t_{diff} = \Delta - \delta/4$ (for half-sine-shaped gradient pulses), and M and M_o = magnetization vector at time = t_{diff} and 0, respectively. Diffusion-sensitive gradient pulses are generally incorporated within a spin-echo pulse sequence.

1.5 Pulse Sequences

1.5.1 Spin Echo

The orientation of the RF coil or antenna is such that the signal collected is proportional to the magnitude of the coherent transverse magnetization in the x-y plane. Normally, a 90^o pulse is used to tip the magnetization vector into x-y plane. After excitation, the M_{xy} magnetization starts to dephase due to the effects described in Eq. 1.12. By applying a 180^o RF pulse, the direction of precession of the M_{xy} magnetization is reversed, which then compensates for the

dephasing of spins due to magnetic field inhomogeneities and/or susceptibility effects. The time interval between the 90^o and 180^o pulses (equal to TE/2; where TE is the Time to Echo) and the repetition time (TR) are generally selected to accentuate signal intensity differences (i.e., create contrast) between various tissues based on differences in the respective T_1 or T_2 relaxation times within the sample [8].

1.5.2 Hahn Spin-Echo (HSE)

The spin-echo pulse sequence was introduced by Hahn in 1950. The MRI version of this pulse sequence is shown in Figure 1-7. At time = 0, a 90^o RF pulse is applied in conjunction with a slice-selective gradient (e.g., G_x) to tip the longitudinal magnetization vector M_z – within a slice – into the x-y plane. After the slice-selective excitation pulse, a rephasing gradient ($-G_x$) is applied (along with phase- (e.g., G_y) and frequency-encoding (e.g., G_z) gradients) to compensate the dephasing effect of slice-selective gradient pulse.

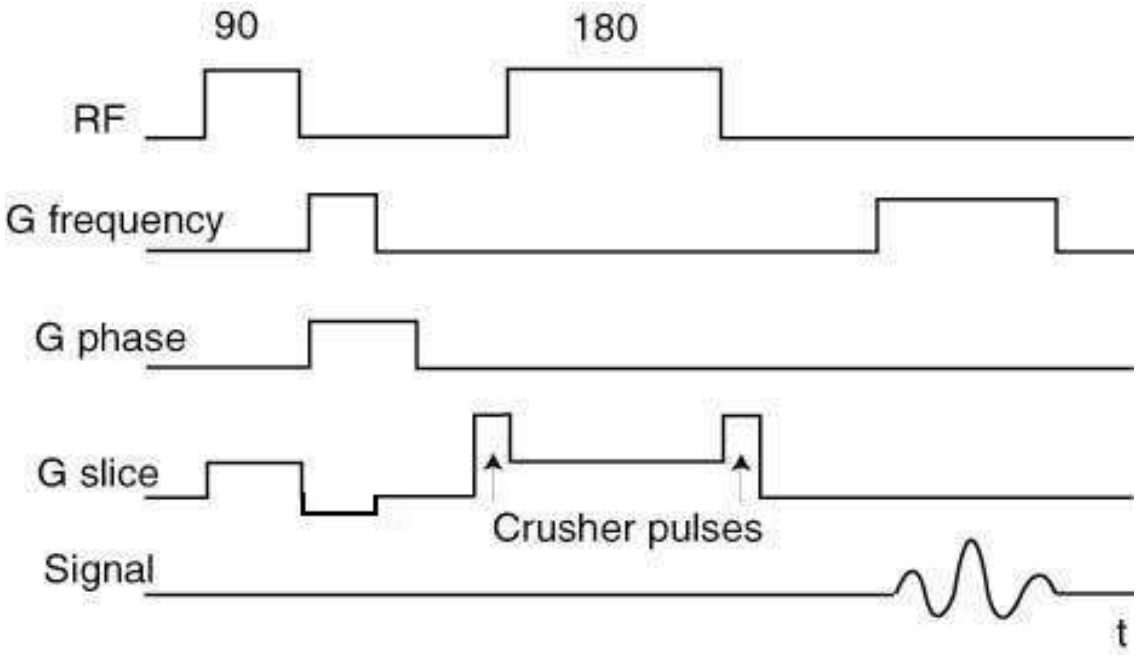

Figure 1-7. Spin-Echo MRI Pulse Sequence (http://www.cis.rit.edu/research/thesis/bs/1999/vangorden/images/timing.jpg).

The 180^o RF pulse is applied TE/2 seconds after 90^o pulse. The signal is detected, in the presence of a readout or frequency-encoding gradient, TE/2 seconds after the 180^o RF pulse. The duration the RF pulses, interval between pulses (TE/2) and repetition time of sequence (TR) define the contrast properties of the image [8].

1.5.3 Carr-Purcell-Meiboom-Gill (CPMG)

To study biomaterial remodeling *in vivo*, calculated T_2 maps are useful for characterizing the process. The data used to generate calculated T_2 maps is obtained from a series of T_2 weighted-images, with varying TE values. However, it can be quite time-consuming to acquire these data using the Hahn spin-echo (HSE) technique, since only one echo is collected at a time. Carr, Purcell, Meiboom and Gill developed a variation of the HSE method in which, following the acquisition of the spin-echo, the transverse magnetization is again refocused by another 180^o RF pulse and another echo is measured (as shown in Figure 1-8; [29]). This process can be repeated for as long as the transverse magnetization persists and is referred to as a multiple SE pulse sequence. The T_2 relaxation time is then calculated from the amplitudes of the train of collected echoes. The effects of RF pulse imperfections can be compensated for by applying the 90^o excitation pulse along the x-axis and the 180^o refocusing pulse along the y-axis of the Cartesian coordinate frame. The T_2 relaxation times are then calculated from the amplitudes of the even-order echoes.

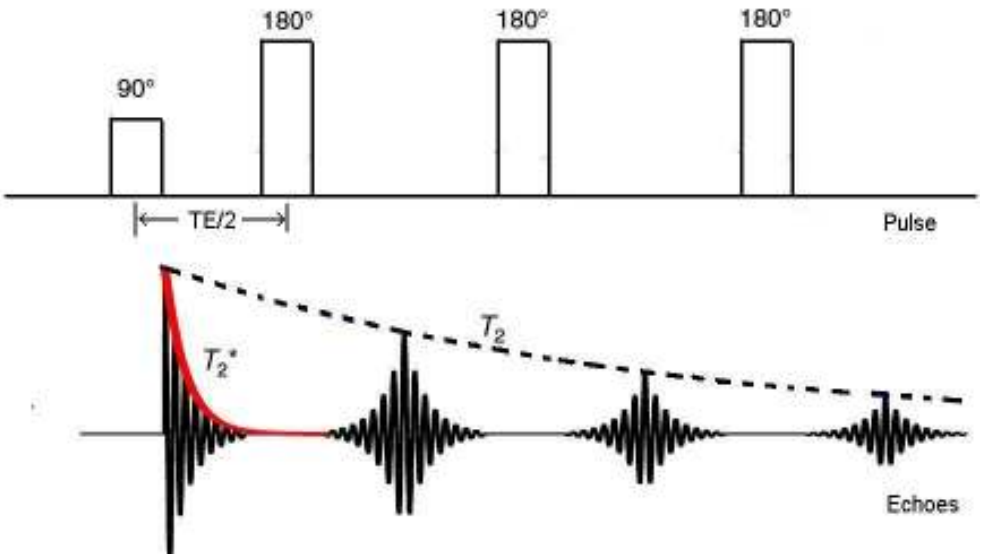

Figure 1-8. Schematic Diagram of the Carr-Purcell-Meiboom-Gill (CPMG) Pulse Sequence [29].

1.6 Surface coils

A surface radiofrequency (RF) coil is a loop of a conducting wire (e.g., copper), which can deliver RF pulses to the sample as well as receive the MRI signal following RF excitation. The primary advantages of surface coil are ease of implementation, spatial selectivity, and localized observation of a specific tissue or organ *in vivo* [30]. Surface-coil sensitivity decreases with depth. Surface coils exhibit good sensitivity to a depth that is on the order of the radius of the coil. The homogeneity and distribution of the RF (B_1) field formed by a surface coil depends upon the geometry and size of the coil as well as the amount of RF power delivered to the coil [31]. The B_1 field variations induced during transmission are mirrored in reception and variations cancel each other [32]. The surface coil exhibits good signal-to-noise ratio (SNR) in the immediate vicinity of the coil and allows the spatial coverage of the coil to be specifically tailored to imaging a particular anatomical region of interest. A model of the single-loop surface coil used in these studies is shown in Figure 1-9. The surface coil is connected to the MRI

system via a coaxial cable. A tuned RF circuit is impedance matched to that of the MRI system (usually 50Ω) to provide efficient RF power transfer to the sample.

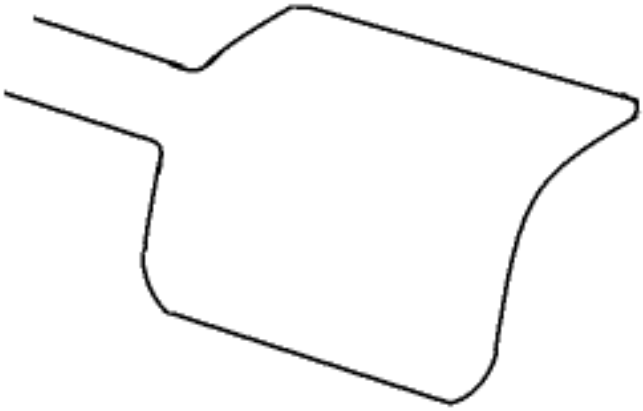

Figure 1-9. Model of Single-Loop Surface Coil Used in These Studies.

2. Introduction to Biomaterials and Applications

Tissue engineering is mainly focused on developing biological substitutes to restore, maintain, improve or replace the tissues or organs that are not functioning adequately [33]. Biomaterials are also used in wound healing, where they work as a temporary cell scaffold/artificial skin and enhance the healing process [34-37] (e.g.: Integra® for skin [38]). The functionality and performance of these biomaterials are evaluated in two different environments: *in vitro* and *in vivo*. For *in vivo* evaluation, the current gold-standard method involves implanting the biomaterial into a living animal and then subsequently harvesting them for immunohistochemical evaluation. This invasive method limits the number of data points that can be collected from a single sample and increases the variability by using different samples from different animals for each time point [28].

The objective of this thesis was to design a non-invasive monitoring system to evaluate biomaterial remodeling *in vivo*. Magnetic Resonance Imaging (MRI) provides such a non-destructive analysis tool that can distinguish changes such as vascularity, cellularity, and water diffusion in soft tissues [10, 12-14, 19-21, 23, 24, 26]. The quantitative nature and possibility of easier evaluation of MRI parameters make MRI a potentially useful methodology that can be applied to monitor the biomaterial *in vivo* to assess the biodegradation process (and may provide results comparable to histological analysis). A nondestructive analysis will increase the statistical robustness of time-series data by facilitating repeated temporal studies of the same implant in a single animal and reducing the intra-animal variability.

Natural (e.g.: collagen, fibrin, albumin and gelatin) and synthetic (e.g.: poly glycolic acid or PGA, Poly ethyl methacrylate or (PEMA)) polymers are used as biomaterials [39-41]. The natural biopolymer, collagen constitutes about 30% of all vertebrae body proteins and provides

structural stability and strength to tissues and organs. Collagen is most abundant in tendons (almost 70%) and in skin (almost 50%). Collagen plays an important role in forming other organs, such as bone, teeth, cartilage and blood vessels; particularly where extreme forces are transmitted. Also, collagen exhibits superior biocompatibility, less antigenicity, and biodegradability when compared to other nature polymers, such as albumin and gelatin [42-44]. Because of these properties, it is widely used for developing biological 3D scaffolds including artificial skin [34, 36], vascular grafts [45-48], wound healing [49], and drug delivery [44] applications. The primary reason for the popularity of collagen as a biomaterial is that it can form extra-strength and biocompatible fibers through its ability to combine with other biomaterials (e.g.: glycosaminoglycan) and crosslinking [44, 45, 50-57]. Because of this, collagen was considered as a suitable biomaterial for these studies.

In this study, collagen sponges with different qualities, such as pore size and biocompatibility, were fabricated using bovine collagen. The sponges were implanted subcutaneously in Sprague-Dawley rats and various MRI parameters, such water T_2, water ADC and MRI-contrast-agent uptake/washout were evaluated in longitudinal time-series studies until the implanted sponges were completely degraded. Sponges were harvested for histological evaluation at each time point in the longitudinal time series. The MRI parameters were correlated with histological data to assess the correspondence between changes in MR images and MRI parameters and changes in cellularity, tissue ingrowth and angiogenesis in the implanted sponges over time. Qualitative histological data was used as a guide to interpret the MRI-parameters results. Using this information, implant biodegradation and physiological outcomes can be evaluated by using repeated MRI temporal studies, which will reduce the number of animals used and increase the statistical robustness of *in vivo* biomaterial evaluation.

2.1 Background

Designing a non-invasive monitoring system to evaluate collagen sponge remodeling *in vivo* requires a brief understanding of the sponge materials, manufacturing techniques and biodegradation process. This section discusses the various properties of the biopolymer used and the methods used to manufacture the scaffolds. The biodegradation process of the implants is also addressed here. Previous studies of the same kind are also discussed.

2.1.1 Sponge Manufacturing

As previously mentioned, collagen is widely used as biomaterial for different biological applications such as artificial skin, tissue and bone replacement, vascular, cartilage, skeletal muscles, cornea and kidney repairs, drug delivery, cell culture and wound dressings [28, 34, 36, 42, 44-49, 55, 58-64]. Since collagen is the major component of the extracellular matrix (ECM) and possesses less antigenicity, it was selected as a suitable biomaterial for this study. Furthermore, the biological and physical properties of collagen can be controlled and modified using biological and chemical processes [51]. Because of its biocompatible nature and the presence of good surface-active agents, collagen sponges are remodeled and integrated with surrounding tissues by natural enzymatic pathways [42, 44]. Collagen biomaterials also enhance new collagen synthesis in the host tissue [49, 55]. The pore structure of collagen scaffolds plays a part in determining the extent of cellular infiltration and nutrient transport through the sponges [43, 64]. A higher resistance to collagen-sponge degradation is generally desired to provide the necessary mechanical strength (in some cases) over time in order to give the body sufficient time to heal itself [53].

2.1.2 Pore Structure

Pore size is the primary determinant of foreign-body responses [63]. There are many techniques such as solvent-casting, gas foaming, melt molding and freeze drying to create and control the size of the pores, the pore structure and pore-interconnection within scaffolds [40, 43]. But most methods, other than freeze drying and gas foaming, involve harsh organic solvents and other treatments that prohibit their use for processing materials for biological applications [40]. Generally, the freeze drying method is used for collagen-sponge fabrication.

During the freeze-drying method, insoluble collagen is prepared in a weak acetic acid solution. This liquid dispersion is then frozen to form ice crystals. The pore size depends on the ice-crystal size, which is a function of the temperature and rate of cooling. The ice crystals are removed by sublimation, which leaves pores in the sponge. Slower cooling results in larger ice crystals and bigger pores whereas faster cooling has the opposite effect. This method generates scaffolds with more than 90% porosity [50, 60, 65]. Non-uniform heat transfer throughout the scaffold causes biomaterial heterogeneity [50]. Also, exposure of skin surface of the scaffold to the atmosphere often results in a surface layer with a different pore structure. As MRI studies need more homogenous scaffolds to simplify the analysis, careful attention was required to control the scaffold properties during fabrication.

2.1.3 Crosslinking

Since collagen is a natural biomaterial, it is very susceptible to natural enzymes, such as metalloproteinases (collagenases), which effectively remove the exogenous material *in vivo* [49]. Various crosslinking techniques are used to bind the collagen molecules, which increases the resistance of the scaffold to biodegradation. Crosslinking improves the mechanical strength and

reduces the immunogenicity of the biomaterial. Physical and chemical crosslinking methods are used to bind the collagen molecules. Chemical crosslinking provides greater control of the degree of crosslinking, as compared to physical methods, which is usually more desirable. Residuals from chemical crosslinking methods can be removed by diligent rinsing. Chemical crosslinking can be performed using glutaraldehyde, formaldehyde, polyepoxy compound, acyl azide, carbodiimides, hexamethylene and chromium tanning [44, 51, 57, 66]. Other than carbodiimides, all chemical agents are incorporated into the chemical bonds between two collagen molecules [44]. Because of this special property of carbodiimide, it is a more suitable chemical crosslinking agent for biological studies.

2.1.4 Carbodiimides

Carbodiimides are highly reactive molecules that can be used to create stable, irreversible bonds [44, 51, 57]. The most commonly used carbodiimide for collagen crosslinking is 1-ethyl-3-(3-dimethylaminopropyl) carbodiimide (EDC). EDC activates the carboxylic acid groups of the protein, primarily on aspartic and glutamic acid residues. These residues react with the amine group of another polypeptide chains, which results in amide bonds. A mild acidic environment is desired for crosslinking, because excess protons are needed to initiate the crosslinking reaction; thus the pH of the crosslinking environment is maintained around 5.0-5.5 [67].

2.1.5 Glycosaminoglycans

Glycosaminoglycans are a class of ECM molecules, which include heparin, heparin sulfate, dermatan sulfate, chondroitin sulfate, hyaluronan and hyaluronic acid [50, 52, 56]. These proteins initiate a signaling cascade within the attached cells and can have a

significant influence on cell behavior. The implants fabricated with collagen and chondroitin sulfate show reduced foreign-body reactions when implanted in subcutaneous tissue [53].

The EDC crosslinking technique also helps to bind other proteins, particularly biocompatible proteins such as glycosaminoglycans (GAGs), with the collagen tripeptide [51]. For these studies, collagen sponges were fabricated to exhibit different, but predictable, tissue responses that would be large enough to be distinguished by MRI. Previous studies have shown that the presence of chondroitin sulfate in scaffolds reduces the inflammatory response, increases the cellular infiltration, decreases the degradation rate, and preserves the sponge pore structure over time [56, 65].

2.2 *In vivo* Implantation

Since the sensitivity of a RF surface coil decreases rapidly as a function of distance from the coil, implanting the scaffolds close to the skin surface is desirable to achieve higher sensitivity (and hence resolution) images. Subcutaneous pockets have become a standard implant location because of the convenience of inserting and removing the scaffolds. A number of earlier studies have used this environment to characterize the tissue and cell responses to scaffolds [68]. Consequently, this model was used to evaluate changes in scaffold remodeling as a function of implantation time, the number of cells around and within the scaffold, new ECM deposition and angiogenesis. These changes were correlated with measured MRI parameters, such as water T_2, water ADC, and degree and rate of MRI-contrast-agent enhancement and dissipation.

2.2.1 Physiological Outcomes

The ultimate purpose of designing a non-invasive technique to monitor the collagen sponges is to provide a general, standard technique, which can be used widely. This study tries to address the fundamental physiological changes and the techniques used to monitor these changes. The following physiological parameters are considered critical design criteria for this thesis: inflammatory response and cell infiltration, angiogenesis, degradation and remodeling, and capsule formation. The above-mentioned physiological parameters have been explored in terms of how they manifest in MRI parameters such as water T_2, water ADC and MRI contrast enhancement. The imaging methods for monitoring these parameters are also defined.

2.2.2 Inflammatory Response and Cell Infiltration

For a monitoring methodology to be useful, it should be able to assess the biocompatibility, cell infiltration, angiogenesis, and extent of implant remodeling. After implantation, an initial inflammatory response takes place because of the presence of the scaffold – a foreign body to native tissue – and because of the surgical wound. This inflammatory response facilitates infiltration by polymorphonuclear cells and macrophages into the scaffold environment [49]. Assessing inflammatory response is needed to predict the later tissue responses and biodegradation. Previous studies have used the T_2 and ADC of water to monitor the cellular distribution and study the heterogeneity of the implanted biomaterials by MRI [14, 69].

2.2.3 Angiogenesis

The depth of cell infiltration inside the scaffold depends on angiogenesis, because cells can survive only few hundred micrometers from the capillaries. The integration between biomaterial and surrounding tissue is ensured by angiogenesis, which regulates transport between the host tissue and the biomaterial [63, 70]. Consequently, the ability of the scaffold to support the development of new blood vessels is considered a critical property. Previous MRI studies have used MRI contrast agents to study angiogenesis [16]. The concentration of the MRI contrast agent in the environment, and time needed to reach the environment after infusion, depends on the vascularity of the scaffold. The changes in MRI-contrast-agent concentration can be studied by comparing the MRI signal intensity changes between pre- and post-contrast T_1-weighted MR images. Generally, a baseline image is acquired before the contrast agent is administered. The contrast agent is then injected and a series of temporally-spaced images are acquired. From these data, the time to reach the maximum (i.e., peak) signal intensity change, relative to the baseline, can be used as an endpoint measure called the **Time-To-Peak (TTP)**. Similarly, the time required for the signal intensity to decline to 50% of this peak value, termed **$T_{1/2}$ (T-Half) Time**, can also be measured [15]. The time-to-peak and $T_{1/2}$ time are expected to decrease with increased angiogenesis due to the presence of a greater number of vessels to transport the MRI contrast agent.

2.2.4 Biodegradation

Cell infiltration and angiogenesis create heterogeneous regions within the scaffold that expand with increased tissue ingrowth. With greater cellular populations within the sponge there is also increased remodeling. Part of the remodeling process is the biodegradation of the sponge

[49], which can be studied using MRI by monitoring the volume changes of the different regions. Preliminary studies have shown that scaffolds with little or no cell infiltration exhibit longer water T_2 values and higher water ADC values (indicative of bulk water) as compared to sponges with cells and other extra-cellular proteins. Based on the relative differences in T_2 relaxation times, information about the cellularity of the scaffold can be obtained [13, 14, 71].

2.2.5 Capsule Formation

Since the scaffold is a foreign body to the tissue, the scaffolds are often encapsulated to protect the surrounding tissue from the foreign material. The thickness of the capsule depends on the biocompatibility of the sponge. Biomaterials exhibiting poor biocompatibility or more antigenicity are generally covered by thicker capsules, which restrict angiogenesis and integration. Consequently, the capsule thickness can be used as an indicator of the biocompatibility of the material [56]. Normally, capsules are composed of dense connective tissues, which restrict translational water movement. These translational restrictions can be assessed by measuring water ADC values, which in turn can be related to the capsule density [69].

2.3 Histology

Heamotoxylin-eosin (H&E) staining is routinely used to study general morphology and cellularity of tissue samples. In the case of biomaterial implants, H&E staining is useful for assessing the extent of cellular infiltration and the overall state of an implant. The differential staining of the nuclei using H&E also allows individual cells to be distinguished; allowing assessment of the total number of cells (or cell density) within the implant.

Other staining methods can be used to detect the presence of specific components within a histological section. For example, Masson's trichrome will stain all collagen structures blue, cell nuclei black, and cytoplasm, muscle fibers and keratin red/pink. This range of colors gives more information about the scaffold, and is particularly useful for detecting collagen. However, the optical-image contrast between the black- and blue-colored stain is often not optimal, so H&E is better suited to cell counting. Blood vessels are more easily distinguished with Masson's trichrome staining.

2.4 Hypotheses

MRI measurement of water T_2 relaxation times, water ADC values, and the degree of MRI contrast enhancement can be used to non-invasively monitor the tissue response to implanted collagen scaffolds, such as cellular infiltration, biodegradation and angiogenesis.

I. The rate of remodeling of collagen sponges *in vivo* can be evaluated non-invasively by monitoring the progressive changes in MR images and MR tissue parameters over time.
    a. Changes in collagen-sponge volume can be quantitatively assessed over time using MR images.
    b. The spatial extent and rate of cellular infiltration of collagen sponges can be quantitatively assessed over time using calculated water T_2 and ADC maps.
    c. The rate of MRI-contrast-agent uptake/washout can be used to assess the spatial extent and degree of angiogenic development within the collagen-sponge implant over time.

II. Differences in resistance to biodegradation and biocompatibility of collagen sponges *in vivo* can be evaluated non-invasively over time using MR images and MR tissue parameters.

   a. Differences in resistance to biodegradation and biocompatibility effects can be quantitatively assessed by measuring differences in collagen-sponge-volume changes over time.

   b. Differences in resistance to biodegradation and biocompatibility effects can be quantitatively assessed by measuring differences in the spatial extent and rate of cell infiltration within the collagen sponge over time.

   c. Differences in resistance to biodegradation and biocompatibility effects associated with angiogenic development can be assessed by evaluating differences in the spatial extent and rate of MRI-contrast-agent uptake/washout within the collagen-sponge implant over time.

3. Materials and Methods

3.1 Sponges Preparation

A 0.8 wt% suspension of bovine flexor tendon collagen (Sigma, Inc.) in 0.25M acetic acid was frozen at -80°C in aluminum trays and lyophilized to fabricate the scaffold [40]. From this sheet of collagen, approximately 1-cm-thick disks, 1.5cm in diameter, were punched. Three types of sponges were fabricated from this starting material in order to vary the biocompatibility and degree of resistance to biodegradation. One of the sponge types was fabricated by crosslinking with 1-ethyl-3-(3-dimethyl aminopropyl) carbodiimide (EDC) to increase the resistance to biodegradation. Chondroitin 6-sulphate (CS) was used with EDC (EDC+CS) to increase the biocompatibility in the second sponge type [52, 72]. In this case, sponges were crosslinked in MES buffer with n-hydroxysuccimide at pH 5.5 [67]. The third sponge type was hydrated in MES buffer only and designated as Uncrosslinked (UnX). Sponges were sterilized by rinsing in 70% ethanol. The physical dimensions of the sponges, particularly the sponge thickness, were reduced after hydration. The UnX sponges are less stiff and exhibit matrix collapse after hydration when compared crosslinked sponges [56]. Figure 3-1 shows the physical appearance of a sponge after lyophilization, but before hydration and crosslinking.

Figure 3-1. Optical Images of Lyophilized Collagen Scaffolds Prior to Hydration and Crosslinking.

3.2 Animal Preparation

The animal protocol for this study was approved by the Institute Animal Care and Use Committee (IACUC) of University of Massachusetts (UMASS) Medical School (IACUC Protocol: A-1759). Eight, 6-7 week-old male Sprague-Dawley rats (250-300g, Charles Rivers Laboratories, Worcester, MA) were used for the study. Rats were anesthetized using a pentobarbital (40mg/1kg, 20mg/ml solution) and xylazine (5mg/Kg, 20mg/ml solution) mix, which was injected intraperitoneally in the left lower quadrant of abdomen. The back of the anesthetized rat was prepped and cleaned with betadine and ethanol solution three times. A 60-mm midline incision was made in the back of the rat using a #3 scalpel handle with a #10 blade. Between the center of the thoracic vertebrae and the center of lumbar vertebrae, three 20-mm-diameter subcutaneous pockets were created on both sides of the incision using a 3.5" hemostat. The distal end of each pocket was not more than 20 mm away from the incision. A hydrated collagen sponge (~15 mm in diameter; ~2-3 mm in thickness) was implanted in each pocket, after dripping off the excess buffer solution. Two sutures were placed on opposite sides of each of each collagen sponge and threaded transcutaneously to avoid movement of the sponge within the subcutaneous pocket over time. To reduce the region differences in tissue response, collagen sponges were implanted close together, but without touching each other [68]. The incision was closed using Ethilon (black monofilament nylon, Ethicon) 4.0 suture material. The rat was placed into a cage to recover from the anesthesia. Figure 3-2 shows the surgical location of the sponges following implantation.

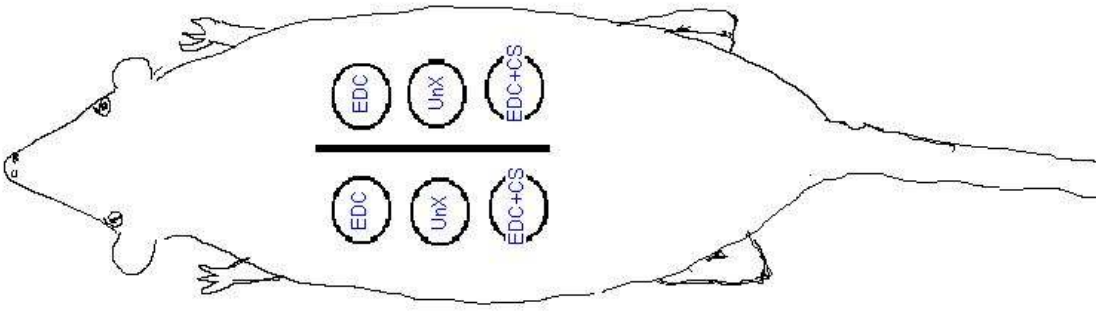

Figure 3-2. Schematic of the Surgical Locations of the Various Collagen-Sponge Implants in the Rat

At 48 hours after surgery (i.e., the Day 2 timepoint) and then once/week for up to 6 weeks, MRI experiments were performed over a 5-6 hour time period. Prior to imaging, the rat was placed in a closed plastic container and administrated 1.5 % Isoflurane for three minutes (or until the animal was fully anesthetized) and then secured in a custom-built animal holder for placement in the magnet. The Lucite animal holder was approximately 50-cm long and 15 cm in diameter (a cylinder). The animal was placed in the prone position on a curved plastic platform in the animal holder. For MRI, a custom-built, surface radiofrequency coil (see Figure 1-9) was positioned on the skin such that it just encompassed the entire set of six collagen sponges. The animal holder was equipped with two air holes at the animal's head for administration of 1.0% Isoflurane in 1.0 L/min breathing-quality air. A hole at bottom of the animal holder served to blow warm air over the animal to maintain the body temperature at 37^{o}C in the magnet. Excess anesthetic gas was vented to the laboratory hood for expulsion.

The MRI contrast agent (MAGNEVIST®; Gadolinium-DTPA) was administered via tail-vein injection at the manufacturer-recommended dose of 0.2 mL/kg (0.1 mmol/kg).

3.3 MRI Measurements

MRI experiments were performed with a Bruker Biospin 2.0T/45cm imaging spectrometer, operating at 85.56 MHz for ^{1}H, with ±20 G/cm self-shielded gradient coils. Multi-slice, T_2-weighted images were acquired using a sagittally-oriented, multiple spin-echo pulse sequence at twelve different echo times (TE = 12, 24, 36, 48, 60, 72, 84, 96, 108, 120, 132, 144 ms) with TR = 2500.0 ms, matrix size = 256 x 128, field of view (FOV) = 6 cm x 4 cm or 6.8 x 4 cm, number of slices = 12-16 (6-8 slices for each side of incision), slice thickness = 2 mm and number of averages = 2. The field of view of each slice covered three sponges on one side of the midline incision and 6-8 contiguous slices were acquired over each set of three sponges so that a quantitative estimate of the total volume could be estimated for each sponge. Since respiratory gating was used to minimize the breathing-motion artifacts in the MR images [73], the duration for a single-slice, T_2-weighted image acquisition (with 12 echoes) was around 16-18 minutes. Thus, the total scan time for acquiring the data for the calculated T_2 maps for all slices was approximately four hours. Figure 3-3 and Figure 3-4 show the field of view and slice orientation of the MR images acquired in this study.

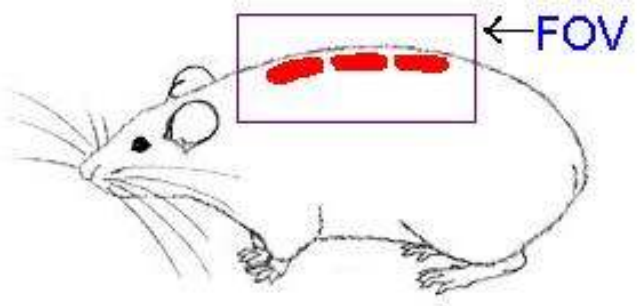

Figure 3-3. Field of View of Sagittal MR Images Acquired in These Studies (red dots just below the rat dorsal surface represent the cross-sectional appearance of the implanted collagen sponges). (* Rat image: http://www.afrma.org/breedimg/ltaillss.jpg).

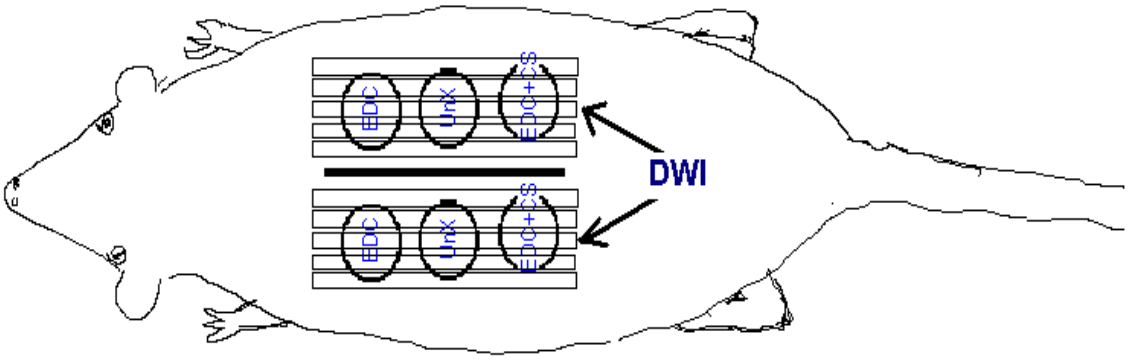

Figure 3-4. Top View of Positions of Sagittal Slices Through Implanted Sponges for T_2 Studies (Diffusion-Weighted Imaging (DWI) was Performed Only at the Middle-Slice Positions on Each Side of the Incision).

Diffusion-weighted MRI (DWI) was performed for only one slice in either side of incision. The DWI slice was positioned to intersect all three sponges on each side of the incision and coincided with the position of one of the slices acquired in the multi-slice, T_2-weighted imaging data sets. DWIs were acquired using a spin-echo, echo-planar imaging pulse sequence. Diffusion-sensitive gradient pulses, with b values = 15, 60, 140, 390, 560, and 760 mm^2 s^{-1}, were applied along each of the three different gradient axes (x, y and z), TR/TE = 2000.0/53.0 ms, matrix size = 64 x 64, slice thickness = 2 mm, number of averages = 2, diffusion gradient separation Δ = 35 ms, diffusion gradient duration δ = 4.0 ms, resulting in a diffusion time $t_{diffusion}$ = 33.7 ms. The total diffusion imaging time was around 25 minutes (i.e., the acquisition of the data along each gradient-axis direction requiring approximately 8 minutes) with respiratory gating applied.

For contrast-agent-enhanced MRI, a pre-contrast image was acquired using a T_1-weighted, spin-echo pulse sequence with TR = 600.0 ms, TE = 10.0 ms, slices = 12-16 (6-8 slices for each set of three sponges on each side of the incision), slice thickness = 2 mm, slice separation = 2.2 mm, and number of averages = 2. The MRI contrast agent (MAGNEVIST®; Gadolinium-DTPA) was administered via tail-vein (intravenous) injection at the manufacturer-

recommended dose of 0.2 mL/kg (0.1mmol/ kg). Post-contrast images were acquired 5 minutes post-injection and then at 10-minutes intervals up to 170 – 240 minutes (or until no significant contrast-enhancement changes were observed). The duration each scan for the contrast-enhanced MRI study, with respiratory gating, was around 7 – 8 minutes.

At the conclusion of each collagen-sponge-remodeling evaluation period (which ranged from 2 days to 42 days), rats were euthanized by intracardiac delivery of a euthanasia solution (with 150-200mg/kg of pentobarbital). The collagen disks were harvested with the surrounding tissue for subsequent histological evaluation and comparison with the corresponding MRI data.

3.4 Data Analysis

ImageJ (Version 1.34s; National Institute of Heath, USA) was used to calculate the T_2 parameter maps from the series of T_2-weighted images. Based on the calculated T_2 values, regions within the calculated T_2 maps of the sponges were segmented (i.e., divided/separated) into regions with short-T_2 and long-T_2 components. The number of pixels in each region within a slice were summed and then multiplied by the slice thickness to estimate the respective sponge volumes associated with the short-T_2 and long-T_2 components for each sponge in the slice. The volumes from all contiguous slices intersecting a particular sponge were then summed to estimate total sponge volume as well as the respective total volumes associated with the short-T_2 and long-T_2 components within the sponge. The average water T_2 values within the respective volumes were then tabulated for subsequent statistical analysis [14].

ADC maps were calculated from diffusion-weighted MR images, using custom software programs written in IDL (Research Systems Inc, Boulder, CO) that were developed by current and former students in the MRI laboratory (Dave Bennett and Erica Henning, respectively) .

The percentage change in signal intensity between pre-contrast (baseline) and post-contrast-enhanced MR images were evaluated using ImageJ. From these data, the time required to attain the maximum signal intensity change was measured as the **Time-To-Peak (TTP)**. Similarly, the time required for the MRI signal intensity to decline to 50% of this peak value was measured as the **$T_{1/2}$ (T-Half) Time** [15, 74]. Figure 3-5 shows the model graph of changes in MRI signal intensity as a function of time post injection of the MRI contrast agent for two separate regions of interest (ROIs) within a single sponge. The MRI parameters TTP and $T_{1/2}$ are indicated on the graph for an ROI at the center of the sponge.

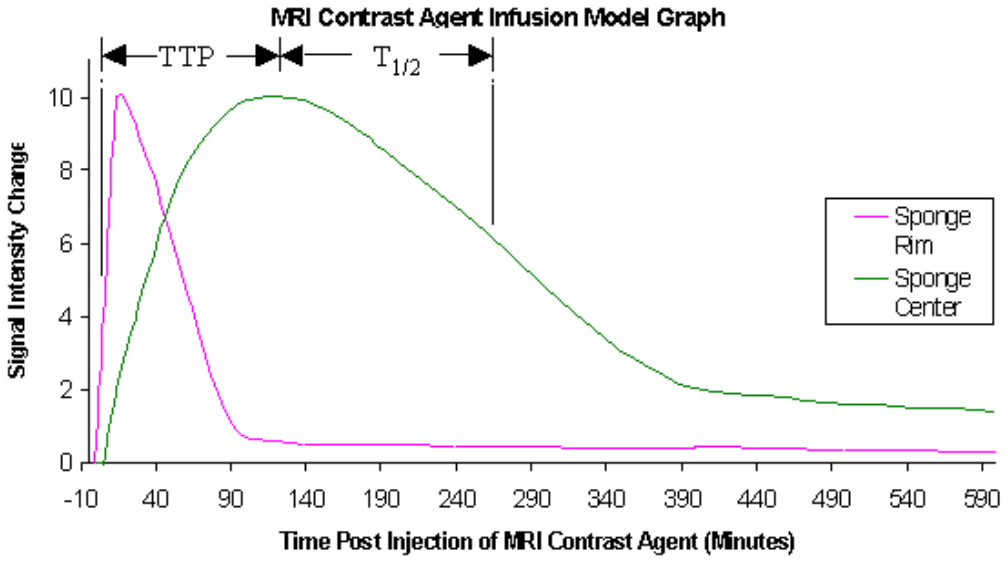

Figure 3-5. MRI Signal Intensity as a Function of Time Post Injection of the MRI Contrast Agent for Two Separate Regions of Interest (rim and center) Within a Single Sponge. The Time Required to Attain the Maximum Signal Intensity Change was Measured as the Time-To-Peak (TTP). The Time Required for the MRI Signal Intensity to Decline to 50% of this Peak Value was Measured as the $T_{1/2}$ (T-Half) Time.

3.5 Histological Analysis

Animals were euthanized and sponges were harvested at each of the imaging time points. Sponges were cut into fourths (perpendicular to the skin surface) and fixed using 10% neutral buffered formalin for paraffin histology. Sections from the middle of the sponge were cut and

stained using Heamotoxylin & Eosin (H&E) and Masson's trichrome. The details of the histological-section preparation and analysis are beyond the scope this thesis. However, images of representative histological sections, which were qualitatively correlated with the MRI data in this study, were collected by Stuart Craig Howes, Graduate Student (2005 - 2007), Worcester Polytechnic Institute, Worcester [75].

3.6 Statistical Analysis

3.6.1. Student's T-test

The one-tailed Student's t-test, assuming unequal variances, was used for statistical comparisons between two data sets. A one-tailed p value less than 0.05 was considered statistically significant. For longitudinal temporal studies (Hypothesis I – changes in MRI-determined parameters within a sponge over time), statistical analyses were carried out by comparing the results from data acquired at different time points with the results obtained at Day 2. For lateral studies (Hypothesis II – differences between sponges at a given time point), the results from each sponge were compared with the results from each of the other two sponges.

3.6.2. Bonferroni Corrections

For temporal studies, six statistical comparisons were performed between the Day 2 data and the data obtained at 7, 14, 21, 28, 35 and 42 days post implantation. In this case, for $\alpha = 0.05$, i.e. 5% critical value for concluding that there is a statistically significant difference, there is an approximately 30% chance (i.e., 6 statistical comparisons X 0.05) of finding a statistical outlier rather than the desired 5% likelihood. This issue was addressed by applying the Bonferroni correction, which multiplies each p value obtained from the Student's t-test by six before

comparing the value with the 0.05 threshold used to assess statistical significance. Similarly, for the three statistical comparisons performed at each time point in the lateral studies, the p value obtained from the Student's t-test was multiplied by three before comparison with the 0.05 threshold [76]. The Bonferroni-corrected p values are tabulated in the Results section and values less than 0.05 were considered statistically significant.

4. Results

4.1 Remodeling and Tissue responses

Figure 4-1 shows a representative calculated T_2 map from one slice (of a multi-slice series) through the center of three sponges implanted on one side of the incision just below the dorsal surface of the rat. The physical boundaries of the three sponges are contained within the field-of-view of the image and each sponge is identified within the tissue matrix. This is the typical presentation for all of the images in the thesis and provides a consistent basis for comparing the results from the water T2, water ADC, and contrast-enhanced MRI studies.

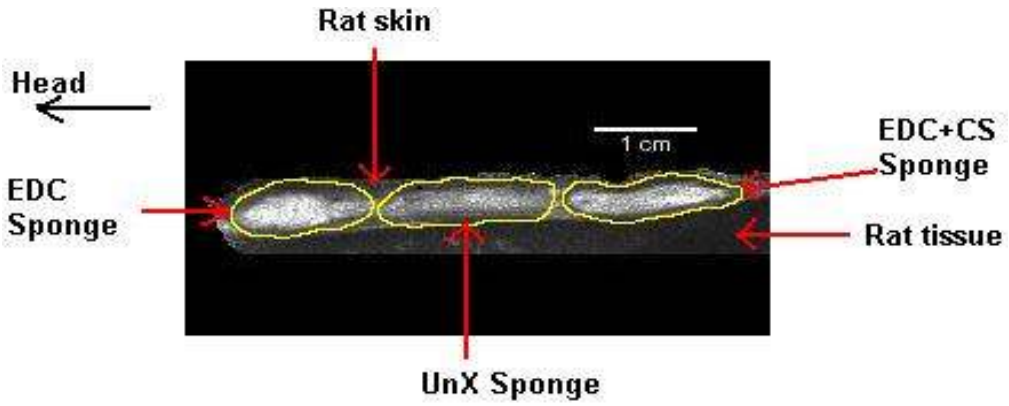

Figure 4-1. Representative Calculated T_2 Map Showing the Implant Locations Within the Rat.

4.1.2 Day 2

Histological images and MRI parameter maps for Day 2 are shown in Figure 4-2 and Figure 4-3. The H&E section from the EDC+CS sponge shows lattice-like lamellae in the cross-linked implant, which appear to form a highly porous interconnecting network occupied primarily by bulk water. The sponge rim appeared to be comprised of a thin layer of infiltrated cells.

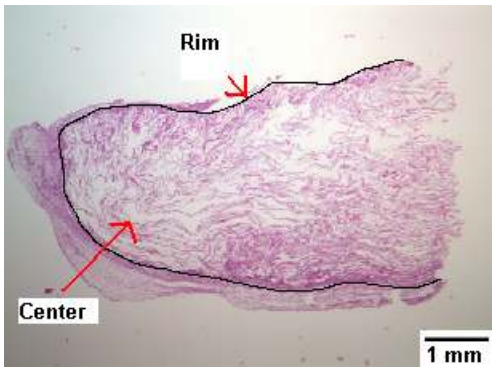

Figure 4-2. H&E Histological Section of EDC+CS Sponge at Day 2.

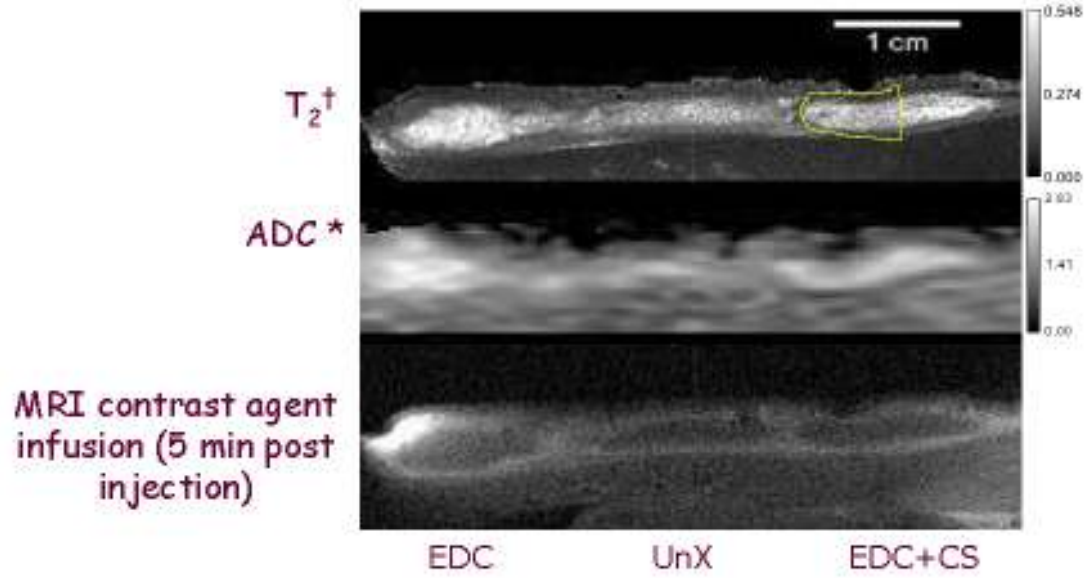

Figure 4-3. Day 2 - MRI Parameter Maps and Post-Contrast-Enhanced MR Image. (T_2 map scale-bar values are in seconds; *ADC map scale-bar values are ADC x 10^{-5} cm^2/s; yellow boundary in T_2 map corresponds to the approximate location from which the histological section was obtained. Histological section and MR images were obtained from different animals.)

For the UnX sponges at Day 2, histological sections showed a less-porous structure (data not shown), and lower water T_2 and water ADC values, as compared to the cross-linked sponges. Calculated T_2 and ADC maps showed a homogenous center within each sponge surrounded by a thin rim. There appeared to be little or no integration between sponges and surrounding tissues. At 5 minutes post-injection, contrast-enhanced MR images showed a thin line of relatively rapid contrast enhancement in the sponge rim. However, MRI contrast agent uptake in the sponge center took a longer time (~120 minutes) and the washout was also significantly delayed as

compared to the rim. Since the histological and MRI data from Day 2 were the least affected by physiological changes following implantation, the Day 2 sponge data was used as the basis of comparison for data acquired at subsequent time points in the temporal study [56].

4.1.3 Day 7

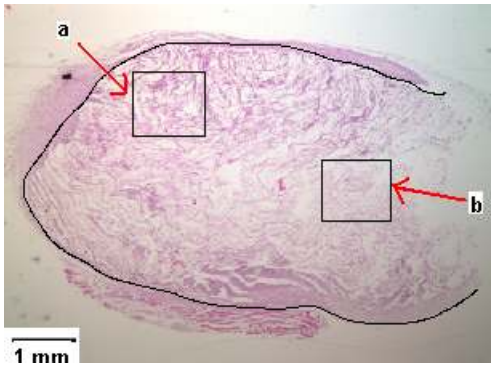

Figure 4-4. H&E Histological Section of EDC+CS Sponge at Day 7 (a. cellular, b. porous).

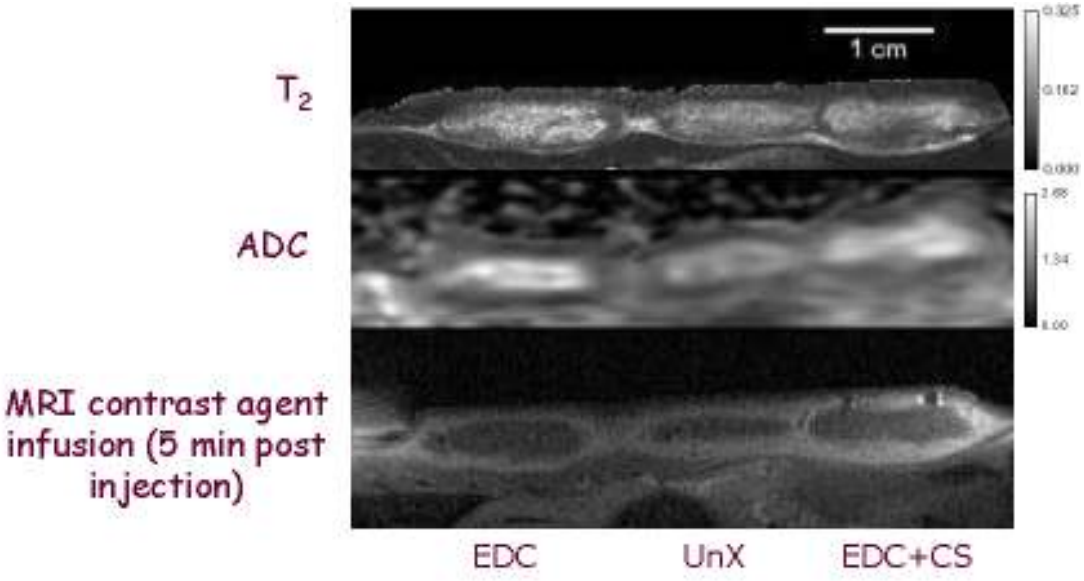

Figure 4-5, Day 7 - MRI Parameter Maps and Post-Contrast-Enhanced Image. (T_2 map scale-bar values are in seconds; *ADC map scale-bar values are ADC x 10^{-5} cm^2/s. Histological section and MR images were obtained from different animals.)

Histological (Figure 4-4) and MR (Figure 4-5) images obtained at Day 7 showed significant volume increases in all three types of sponges; presumably due to an inflammatory response. Cellular infiltration was found in the sponge rims of H&E-stained sections and MR images showed lower water T_2 and ADC values in approximately the same regions. The spatial distribution of water T_2 and ADC values within the sponge was more heterogeneous at Day 7 as compared to Day 2. UnX sponges showed a greater extent of cellular infiltrations in the rim region as compared to cross-linked sponges at the same time point. A thin capsule also appeared to form around the implant rims at Day 7. The post-contrast-enhanced MR images showed a thicker rim of contrast enhancement at 5 minutes post-injection. The contrast-agent uptake time was shorter than at Day 2, but there was no apparent difference in washout time for cross-linked sponges.

4.1.4 Day 14

Figure 4-6 and Figure 4-7 show the respective histological and MR images obtained at Day 14, where the volumes of all sponges decreased relative to Day 7. In general, sponges exhibited more heterogeneous and lower water T_2 and ADC values. In the histological sections, the sponge rim showed a high degree of cellular infiltration and the sponge center showed little remaining porous and/or lamellar structure. The implants were surrounded by capsules, which showed lower ADC values when compared to the center of the sponges. There was a significant increase in the rate of contrast agent update and washout in the sponge centers. The volume of the sponge center was reduced compared to that observed in previous weeks.

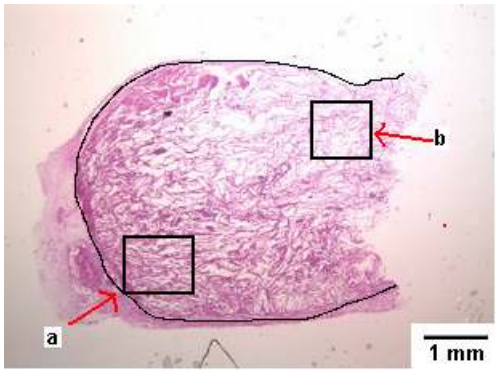

Figure 4-6. H&E Histological Section of EDC+CS Sponge at Day 14 (a. more cellular, b. more porous).

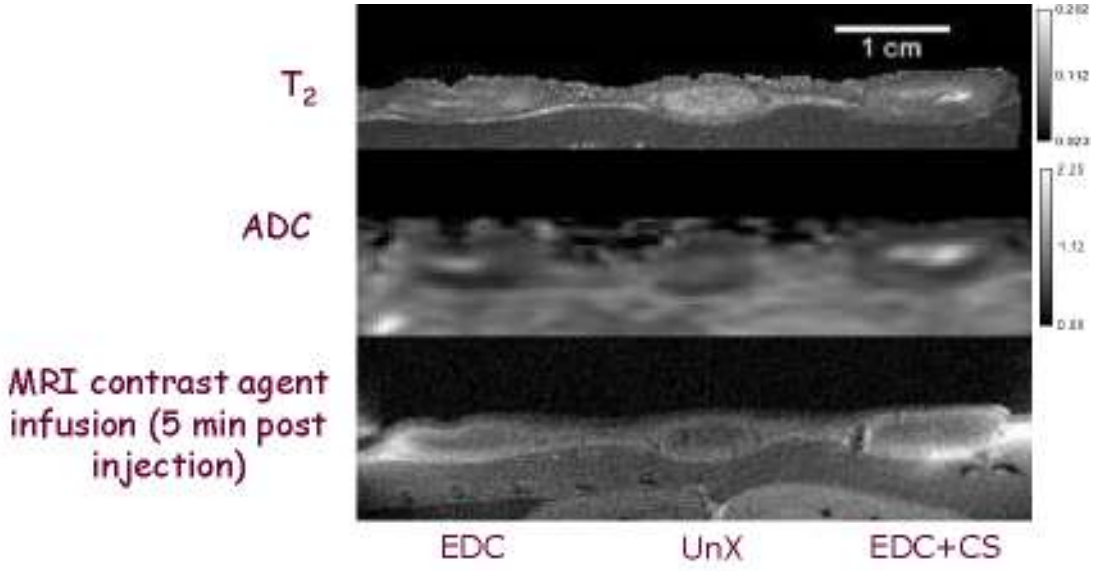

Figure 4-7. Day 14 - MRI Parameter Maps and Post-Contrast-Enhanced Image. (T_2 map scale-bar values are in seconds; *ADC map scale-bar values are ADC x 10^{-5} cm^2/s. Histological section and MR images were obtained from different animals.)

4.1.5 Day 21

The sponges looked more homogeneous at Day 21 in both histological (Figure 4-8) and MR images (Figure 4-9) because of complete infiltration of cells into the sponges. No porous or lamellar matrix structures were found in histological sections at Day 21. A significant decrease in volume was observed for all three sponge types. Calculated water T_2 and ADC maps were consistent with increased cellularity and showed uniformly reduced values throughout the

sponge volume. The capsule appeared to be resorbed and sponges were integrated with the surrounding tissue. Contrast-agent uptake and washout times were further reduced as compared to previous weeks; consistent with increased vascularity in the regions of cellular infiltration. Most of the UnX sponges were biodegraded by Day 21.

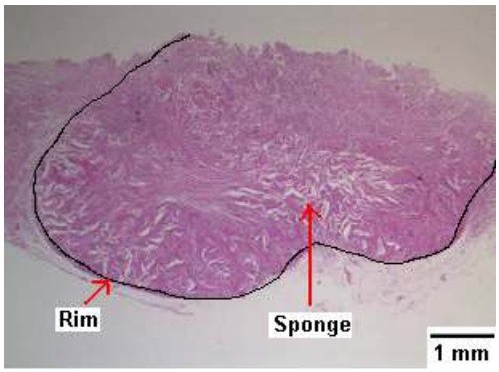

Figure 4-8 H&E Histological Section of EDC+CS Sponge at Day 21.

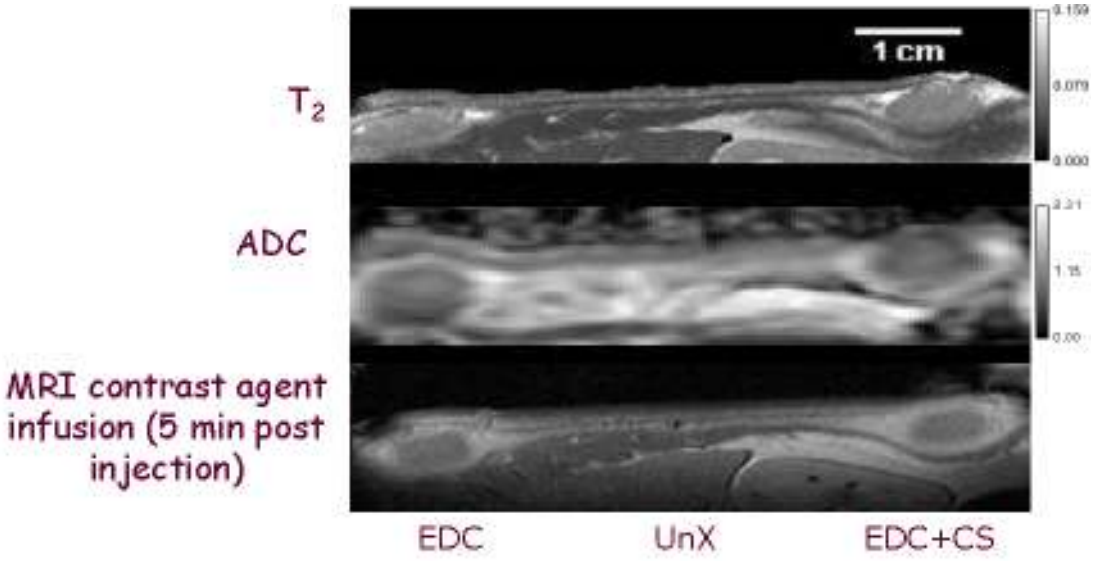

Figure 4-9. Day 21 - MRI Parameter Maps and Post-Contrast-Enhanced Image. (T_2 map scale-bar values are in seconds; *ADC map scale-bar values are ADC x 10^{-5} cm^2/s. Histological section and MR images were obtained from different animals.)

4.1.6 Day 28

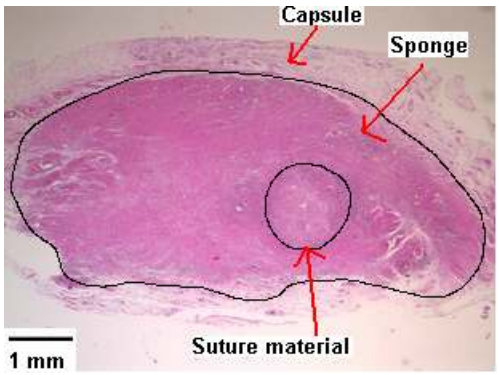

Figure 4-10. H&E Histological Section of EDC+CS Sponge at Day 28.

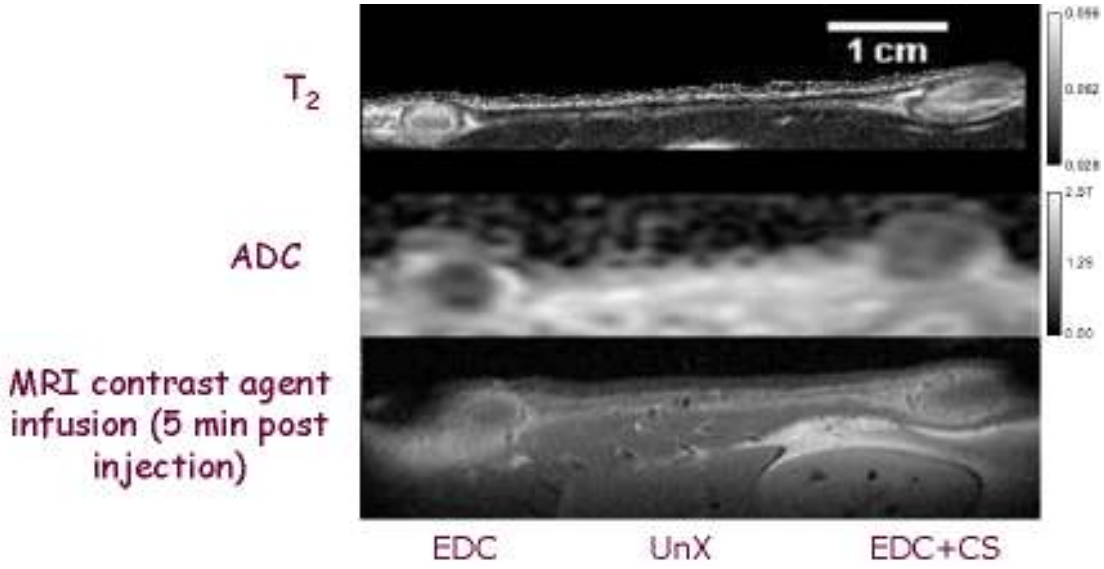

Figure 4-11. Day 28 - MRI Parameter Maps and Post-Contrast-Enhanced Image. (T_2 map scale-bar values are in seconds; *ADC map scale-bar values are ADC x 10^{-5} cm^2/s. Histological section and MR images were obtained from different animals.)

By Day 28, the histological images (Figure 4-10) showed a more homogenous sponge interior; consistent with complete cellular infiltration and an implant that is well integrated with surrounding tissues. No UnX sponges were harvested at Day 28 (or beyond) and MR images and MRI parameter maps (Figure 4-11) confirmed the complete absence of the sponges. EDC sponges degraded more rapidly as compared to EDC+CS sponges. Calculated water T_2 and ADC maps showed moderate heterogeneity between the sponge center and the rim. Contrast

agent studies showed shorter uptake and washout times for both the sponge centers and rims as compared to earlier time points. Post-contrast images taken at 5 minutes post-injection showed that the area of the sponge center was smaller than that of the rim.

4.1.7 Day 35

Figure 4-12. H&E Histological Section of EDC Sponge at Day 35.

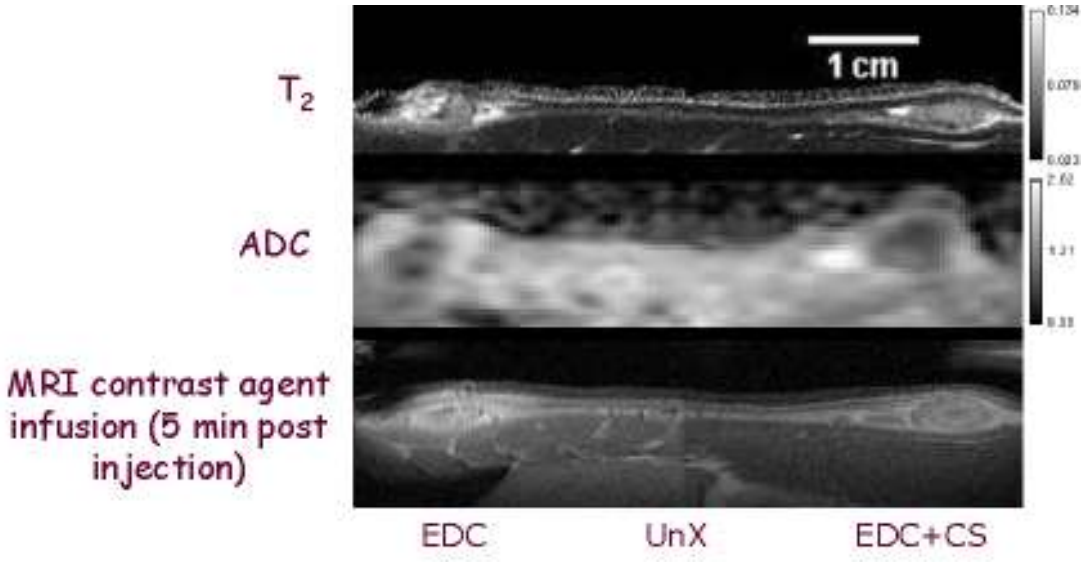

Figure 4-13. Day 35 - MRI Parameter Maps and Post-Contrast-Enhanced Image. (T_2 map scale-bar values are in seconds; *ADC map scale-bar values are ADC x 10^{-5} cm^2/s. Histological section and MR images were obtained from different animals.)

Histological images of cross-linked sponges (Figure 4-12) obtained at Day 35 showed homogenous staining, similar to that observed at Day 28. Most of the EDC sponges were

completely degraded by Day 35. From the MR measurements (Figure 4-123), the T_2 and ADC values were relatively unchanged as compared with those obtained at Days 28 and 21. The MR images of the sponges were homogeneous and exhibited a much smaller implant volume. MRI contrast-enhancement studies showed shorter uptake and washout times in the sponge centers, similar to those observed in the sponge rims.

4.1.8 Day 42

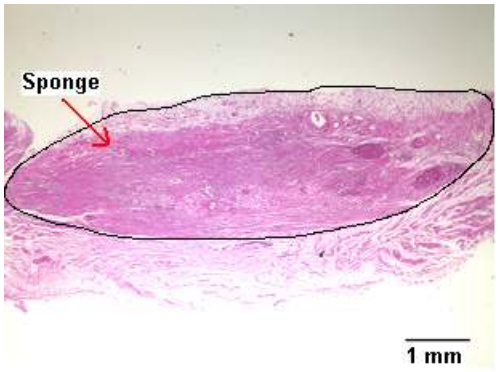

Figure 4-14. H&E Histological Section of EDC+CS Sponge at Day 42.

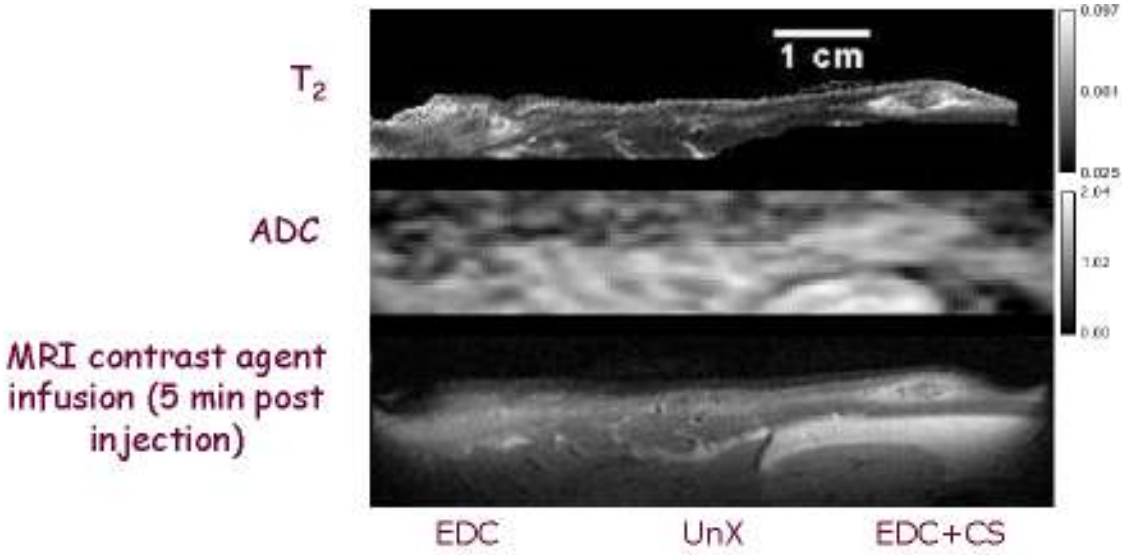

Figure 4-15. Day 42 - MRI Parameter Maps and Post-Contrast-Enhanced Image. (T_2 map scale-bar values are in seconds; *ADC map scale-bar values are ADC x 10^{-5} cm^2/s. Histological section and MR images were obtained from different animals.)

Histological sections (Figure 4-14) showed that the physiological conditions on the sponge were similar to those observed at Day 35; although with a reduction in sponge volume. No sponges were identified in calculated ADC maps (Figure 4-15) and only small residual volumes of EDC+CS sponges were found in the calculated T_2 maps. In the contrast-agent studies, no sponge center was identified in the image obtained at 5 minutes post-injection. Most of the sponges were biodegraded at Day 42 and this was the last experiment point for this study. The quantitative MR measurements obtained for the sponges studied at each time point in the temporal study are summarized below.

4.2 Volume Changes for EDC+CS Sponges as a Function of Implantation Time

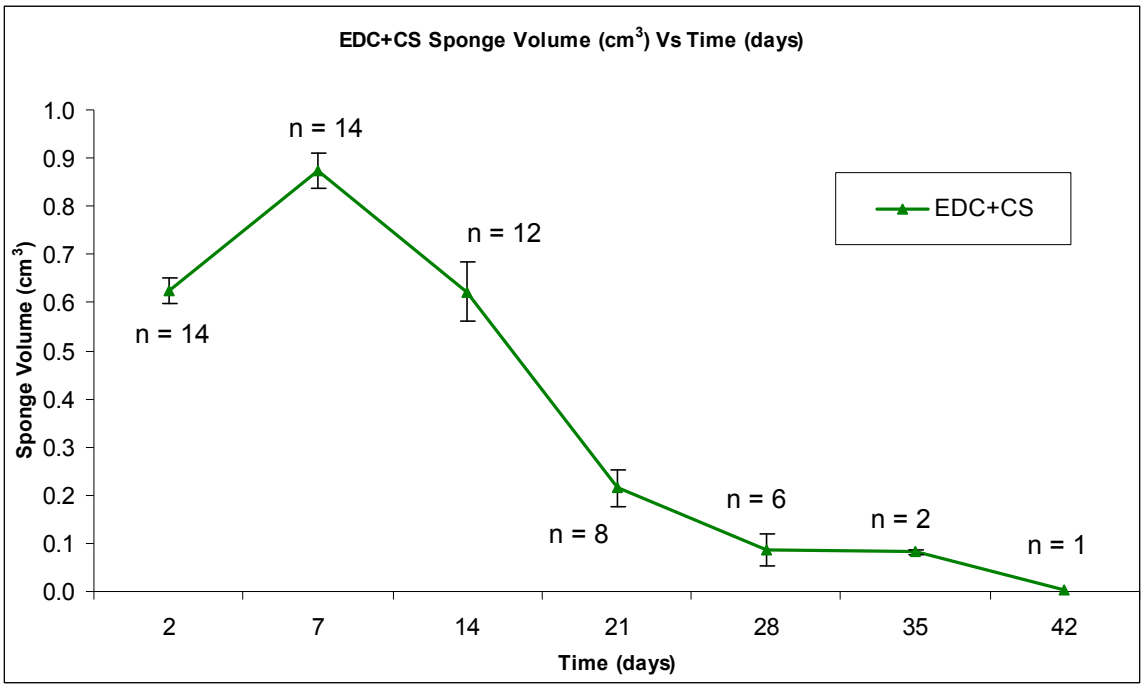

Figure 4-16. Changes in EDC+CS Sponge Volume as a Function of Implantation Time (n = number of sponge samples; error bars represent SEM).

Figure 4-16 shows the volume changes of the EDC+CS collagen sponges as a function of implantation time. The total volume of the sponge decreased with increasing implantation time. There was an increase in volume at Day 7 (presumably due to inflammatory processes), which then started to decrease beginning at Day 14. Complete biodegradation occurred after 42 days for the EDC+CS cross-linked sponges. Changes in sponge volume, relative to Day 2, were significant after Day 14 ($p < 0.0001$). The statistical analyses were done by comparing data from each of the later time points (i.e., Days 7, 14, 21, 28, 35 and 42) with the Day 2 data. The detailed results of the statistical analysis (with Bonferroni corrections) and the number of sponges studied at each time point are given in Table 4-1. The volume changes in MR images are shown in Figure 4-17.

Table 4-1. Statistical Results for Changes in EDC+CS Sponge Volume as a Function of Implantation Time (n/a: not applicable because of insufficient data due to sponge degradation).

Comparison	Day 7	Day 14	Day 21	Day 28	Day 35	Day 42
p (within EDC+CS) (n = 14 @ Day 2)	3.7E-05 (n = 14)	1.0 (n = 12)	9.7E-07 (n = 8)	1.5E-07 (n = 6)	4.7E-11 (n = 2)	n/a (n = 1)

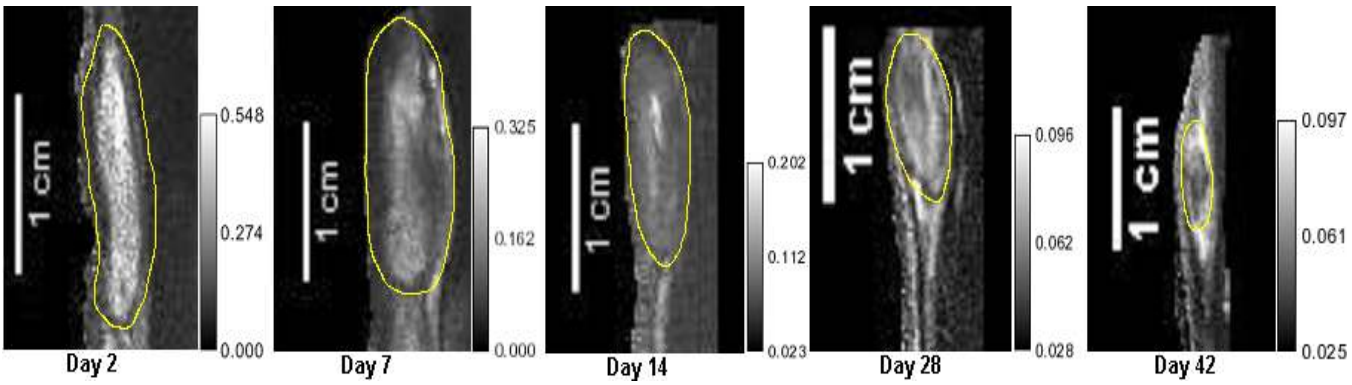

Figure 4-17. Changes in EDC+CS Sponge Volume as a Function of Implantation Time. (Units on the T_2 gray scale bars are in seconds. Example images were obtained from different animals at different time points. Regions inside yellow boundaries delineate the sponges.)

4.3 Changes in T_2 Values in EDC+CS as a Function of Implantation Time

The T_2 relaxation time values of EDC+CS sponges showed a decreasing trend after implantation with slight increase after Day 28 (Figure 4-18). Beginning at Day 7, and at all time points thereafter, T_2 values within the sponges were significantly reduced as compared to Day 2 ($p < 0.0001$). After Day 21, the T_2 values plateaued at a relatively constant value until Day 42. The statistical results for all of the EDC+CS T_2 data are given in Table 4-2.

Table 4-2. Statistical Results for Changes in EDC+CS Sponge T_2 Values as a Function of Implantation Time (n/a: not applicable because of insufficient data due to sponge degradation).

Comparison	Day 7	Day 14	Day 21	Day 28	Day 35	Day 42
p (within EDC+CS) (n = 16 @ Day 2)	0.09 (n = 14)	1.5E-06 (n = 12)	1.6E-08 (n = 8)	3.6E-09 (n = 6)	7.5E-08 (n = 2)	n/a (n = 1)

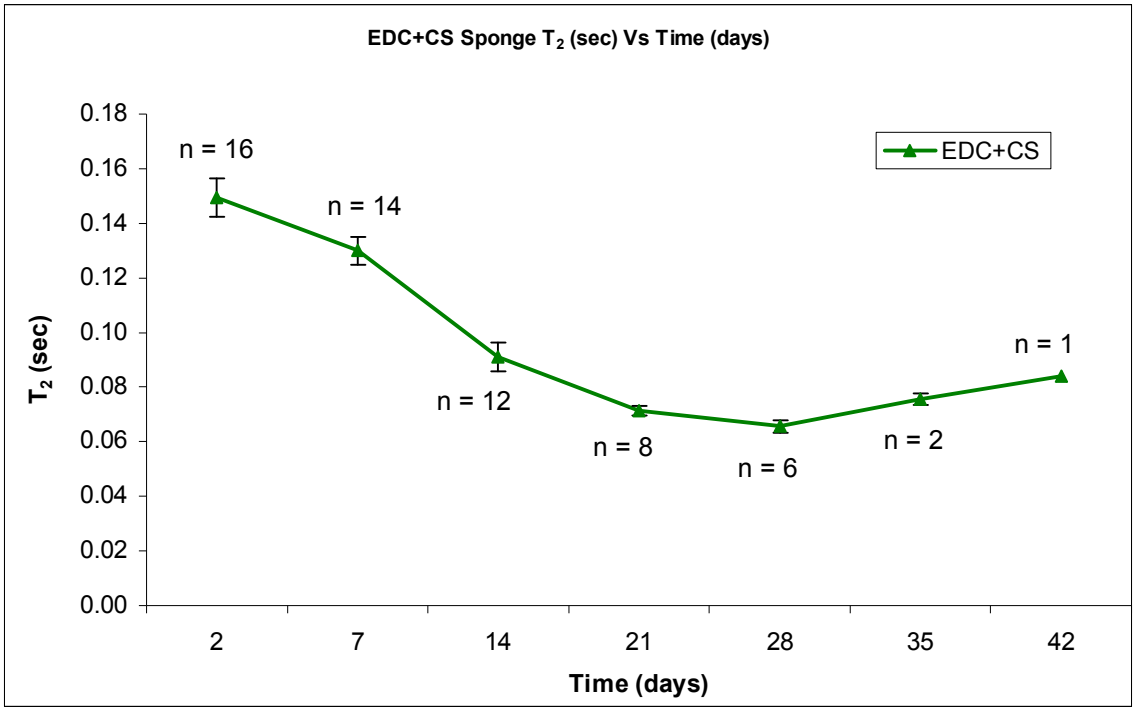

Figure 4-18. Changes in EDC+CS Sponge T_2 Values as a Function of Implantation (n = number of sponge samples; error bars represent SEM).

4.4 Changes in Water Apparent Diffusion Coefficient (ADC) Values in EDC+CS Sponges as a Function of Implantation Time

Similar to the trend observed for T_2, the water ADC values for EDC+CS sponges decreased progressively after implantation; consistent with an increase in cellular infiltration. The water ADC values were significantly reduced (as compared to the Day 2 values) at Day 7 and all time points thereafter. After Day 21, the water ADC values maintained a constant value, indicating that complete cellular infiltration had been attained at that time point.

Table 4-3 gives all of the statistical results of the EDC+CS ADC measurements over time. Figure 4-19 shows the how the water ADC values for EDC+CS sponges changed over time. Representative calculated water ADC maps of EDC+CS sponges, at various points in the time series, are shown in Figure 4-20.

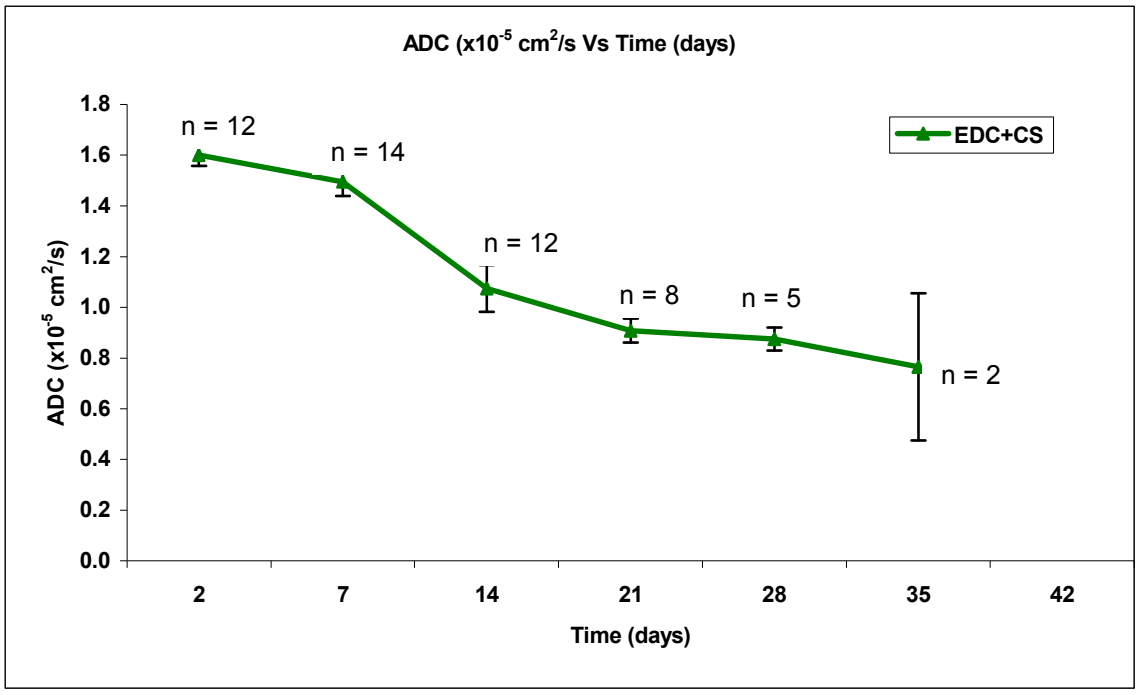

Figure 4-19. Changes in EDC+CS Sponge Water ADC Values as a Function of Implantation (n = number of sponge samples; error bars represent SEM).

Table 4-3. Statistical Results for Changes in EDC+CS Sponge Water ADC Values as a Function of Implantation Time (n/a: not applicable because of insufficient data due to sponge degradation).

Comparison	Day 7	Day 14	Day 21	Day 28	Day 35	Day 42
p (within EDC+CS) (n = 12 @ day 2)	0.4 (n = 14)	3.1E-04 (n = 12)	2.3E-08 (n = 8)	4.2E-07 (n = 5)	0.6 (n = 2)	n/a (n = 0)

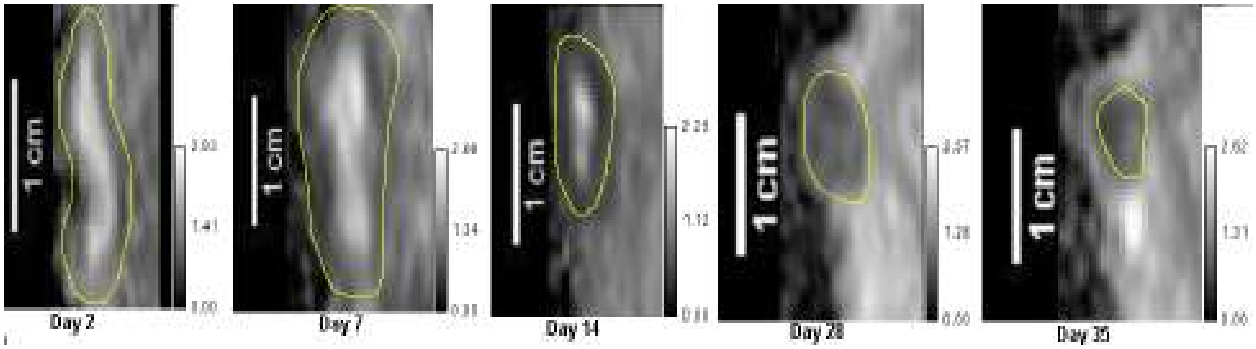

Figure 4-20. Changes in EDC+CS Sponge Water ADC Values as a Function of Implantation Time. (Units on the ADC gray scale bars are: ADC x 10^{-5} cm^2/s. Example images were obtained from different animals at different time points. Regions inside yellow boundaries delineate the sponges.)

4.5 MRI Contrast Enhancement Study Results

4.5.2 Contrast-Enhancement Changes in EDC+CS Sponges as a Function of Implantation Time

Contrast-enhanced MR images of the EDC+CS sponges were subdivided into two regions of interest (ROIs): the sponge center and sponge rim. Figure 4-21 illustrates the locations of both ROIs for the Day 2 and Day 21 data. The overall signal intensity changes in these slices over time (5 minutes to 180-240 minutes) are shown in Figure 4-22 and Figure 4-23 for the Day 2 and Day 21 data, respectively. For a given time series, the signal intensity within each of the ROIs (sponge center and rim) was integrated at each time point. The process was then repeated for each slice that intersected a particular sponge (6-8 slices), with center and rim ROIs that were individually determined for each slice.

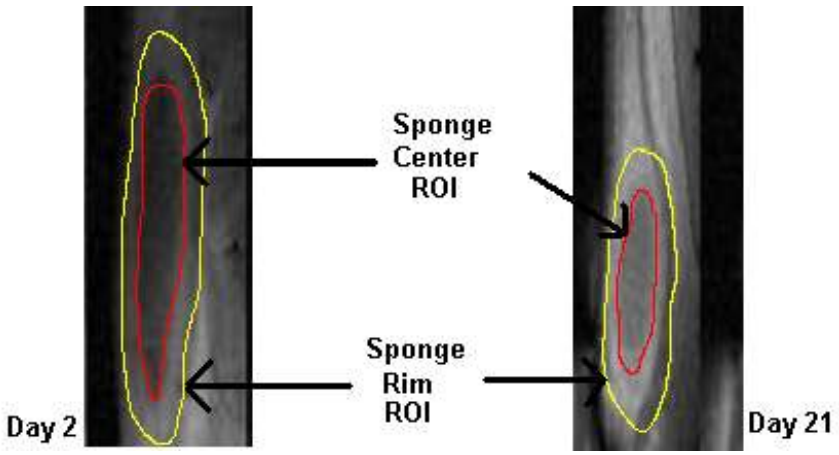

Figure 4-21. Region of Interest (ROI) Delineation for EDC+CS Sponge Center and Rim in Contrast-Enhanced MR Images Obtained 5 Minutes Post-Injection of a MRI Contrast Agent. (Yellow boundaries demarcate the total sponge areas in the slice. Red boundaries demarcate the sponge center and the area between the red and yellow boundaries demarcate the sponge rim region.)

For a given sponge, the signal intensity from the respective center and rim ROIs for each slice were then summed over all slices to give the total signal intensity for each ROI. Total signal-intensity comparisons between pre- and post-contrast time points were then calculated for each ROI and reported as the percent signal intensity change within the ROI as a function of time after the injection of the MRI contrast agent. Plots of these data are shown in Figure 4-24 and Figure 4-25 or the Day 2 and Day 21 data, respectively. From these plots, Time-To-Peak and $T_{1/2}$ time were measured for the ROIs in each sponge.

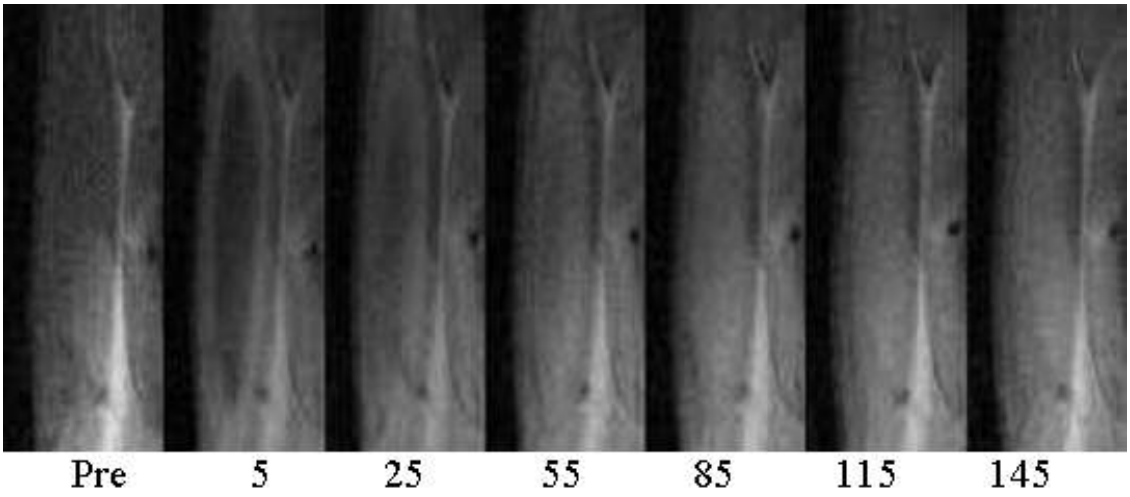

Figure 4-22. T_1-weighted MR Images of EDC+CS Collagen Sponge as a Function of Time Post-Injection of an MRI Contrast Agent at Day 2 Following Implantation.

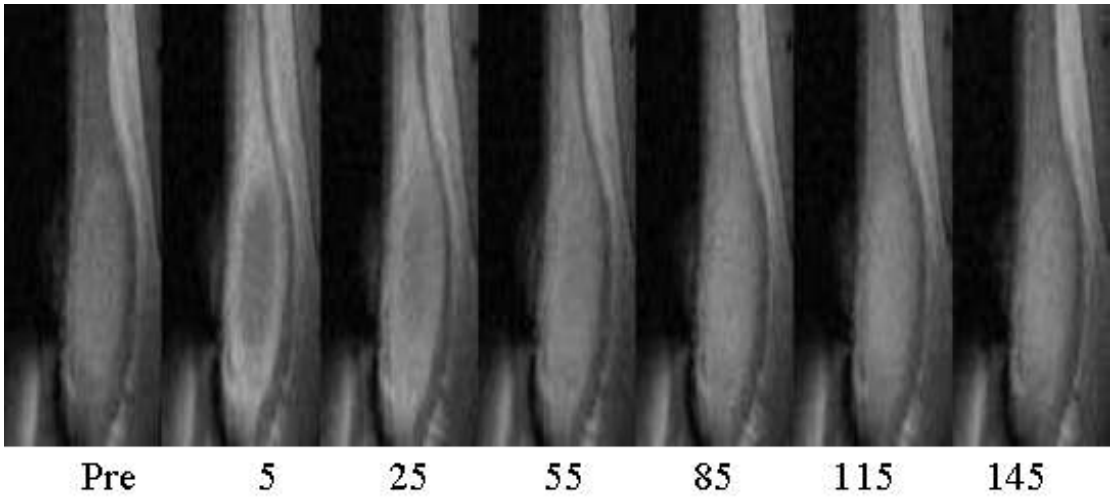

Figure 4-23. T_1-weighted MR Images of EDC+CS Collagen Sponge as a Function of Time Post-Injection of an MRI Contrast Agent at Day 21 Following Implantation.

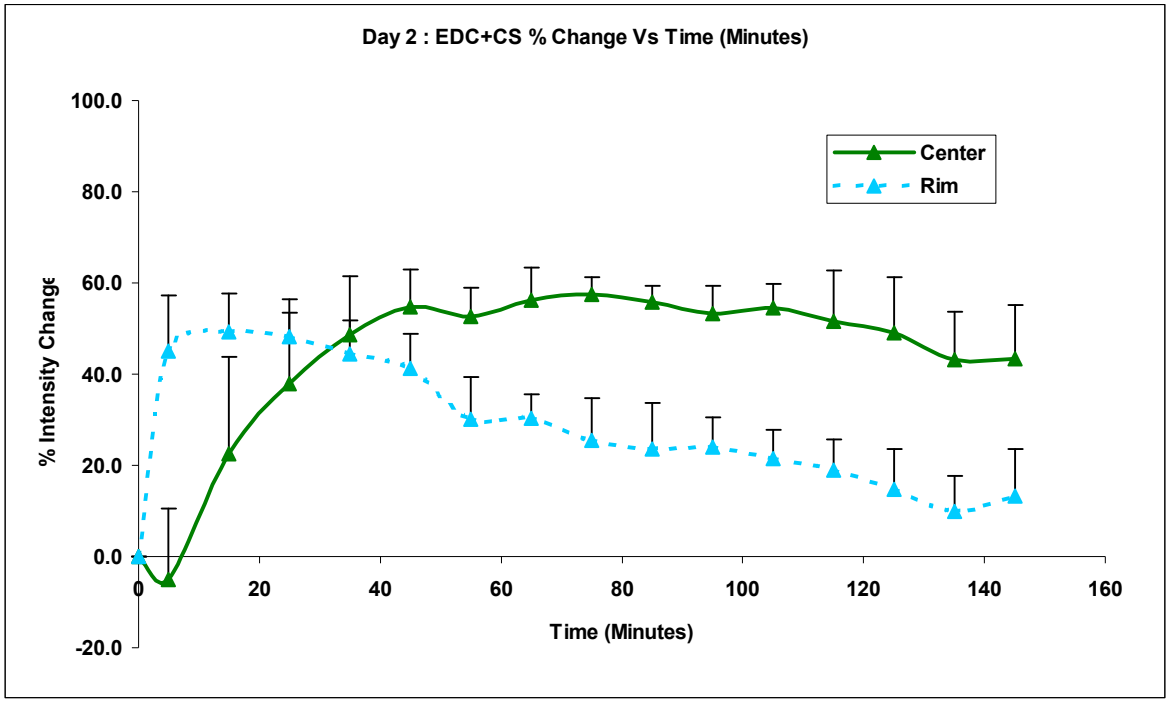

Figure 4-24. Plot of Percent Signal Intensity Change within Center and Rim ROIs of EDC+CS Sponges as a Function of Time after Injection of an MRI Contrast Agent at Day 2 Following Implantation.

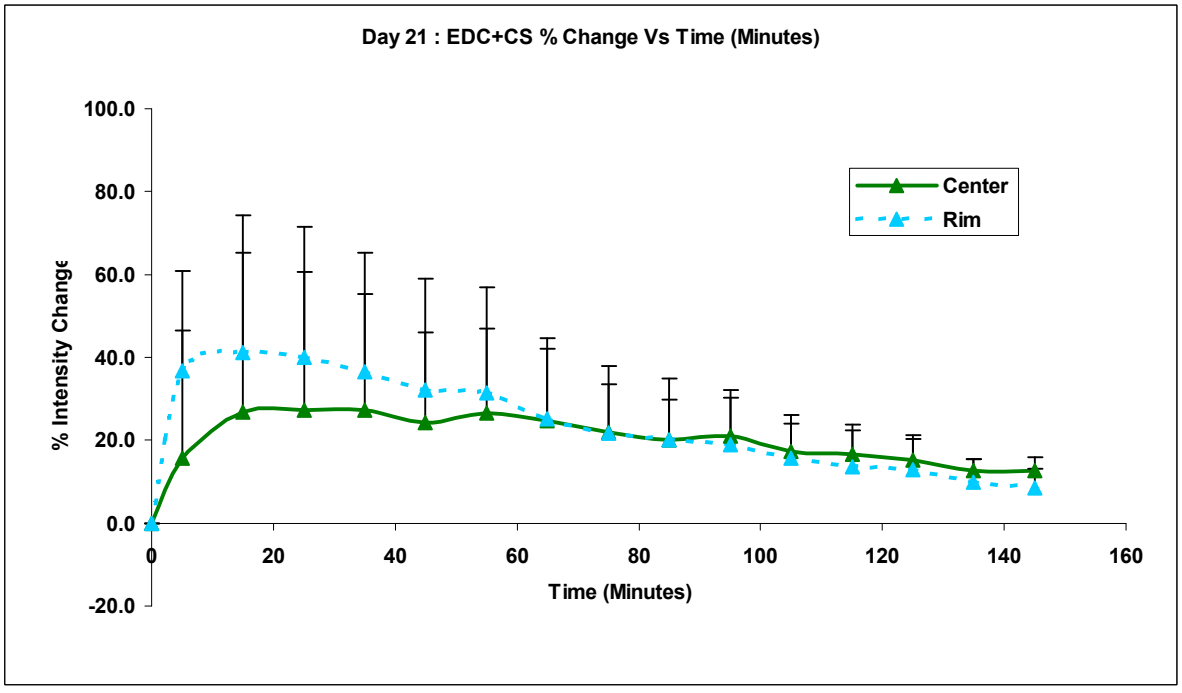

Figure 4-25. Plot of the Percent Signal Intensity Change within Center and Rim ROIs of EDC+CS Sponges as a Function of Time after Injection of an MRI Contrast Agent at Day 21 Following Implantation.

4.5.3 Changes in Time-To-Peak (TTP) Values for EDC+CS Sponges as a Function of Implantation Time

Plots of the mean TTP values in the center and rim ROIs of the EDC+CS sponges as a function of implantation time are shown in Figure 4-26 (a) and (b). Time-to-peak values showed a decreasing trend in the sponge center, while the "rim" regions of the scaffold showed no significant changes as a function of time post-implantation. The statistical results for the TTP data are shown in Table 4-4. The changes in TTP were significant after Day 14 as compared to Day 2 ($p < 0.02$). The rim region of the sponge showed lower, but fairly constant, TTP values at all time points.

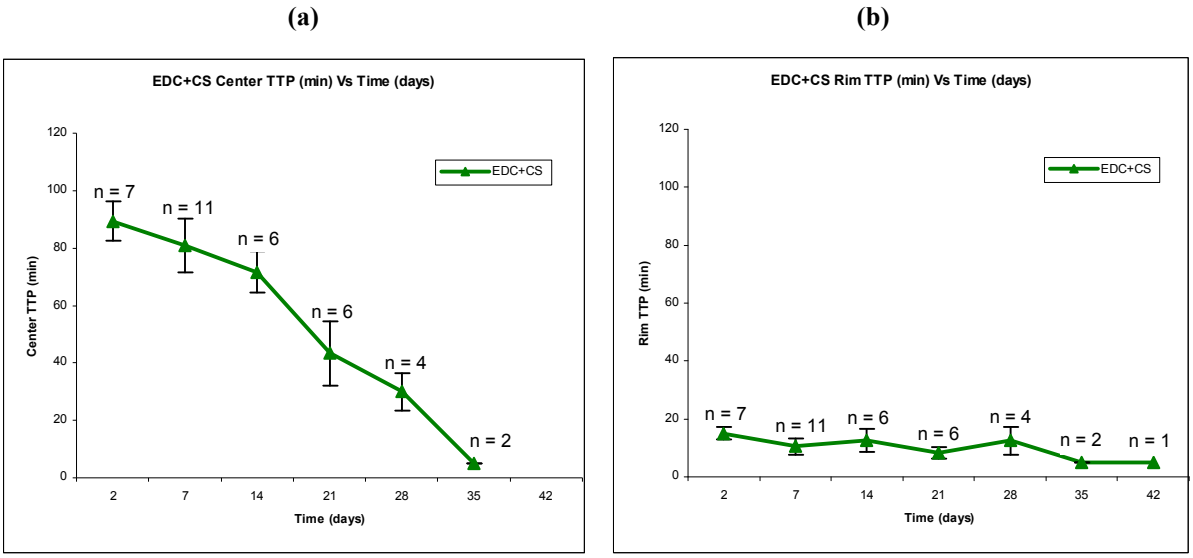

Figure 4-26. Plots of the Mean TTP Values in the Center (a) and Rim (b) ROIs of the EDC+CS Sponges as a Function of Implantation Time (n = number of sponge samples; error bars represent SEM).

Table 4-4. Statistical Results for TTP Values in the Center ROI of the EDC+CS Sponges as a Function of Implantation Time (n/a: not applicable because of insufficient data due to sponge degradation).

Comparison	Day 7	Day 14	Day 21	Day 28	Day 35	Day 42
p (within EDC+CS) (n = 7 @ Day 2)	1.0 (n = 11)	0.3 (n = 6)	0.02 (n = 6)	0.001 (n = 4)	5.3E-05 (n = 2)	n/a (n = 0)

4.5.4 Changes in $T_{1/2}$-Time Values for EDC+CS Sponges as a Function of Implantation Time

The mean $T_{1/2}$-time values in the rim and center ROIs of the EDC+CS sponges as a function of implantation time are shown in Figure 4-27 (a) and (b). The $T_{1/2}$-time value in the sponge center was significantly reduced at Day 28, as compared to Day 2 ($p < 0.02$), but no significant differences were seen at the other time points (Figure 4-27a). No statistically significant changes in the $T_{1/2}$-time values, relative to the value at Day 2, were observed in the sponge rim at any time point (Figure 4-27b). The statistical results for the $T_{1/2}$-time values in the EDC+CS sponge center are shown in Table 4-5. Both the TTP and $T_{1/2}$-time parameters exhibited similar trends over time in the EDC+CS sponges. At the early time points (< Day 14), the TTP and $T_{1/2}$-time parameters were unchanged in the sponge center and rim.

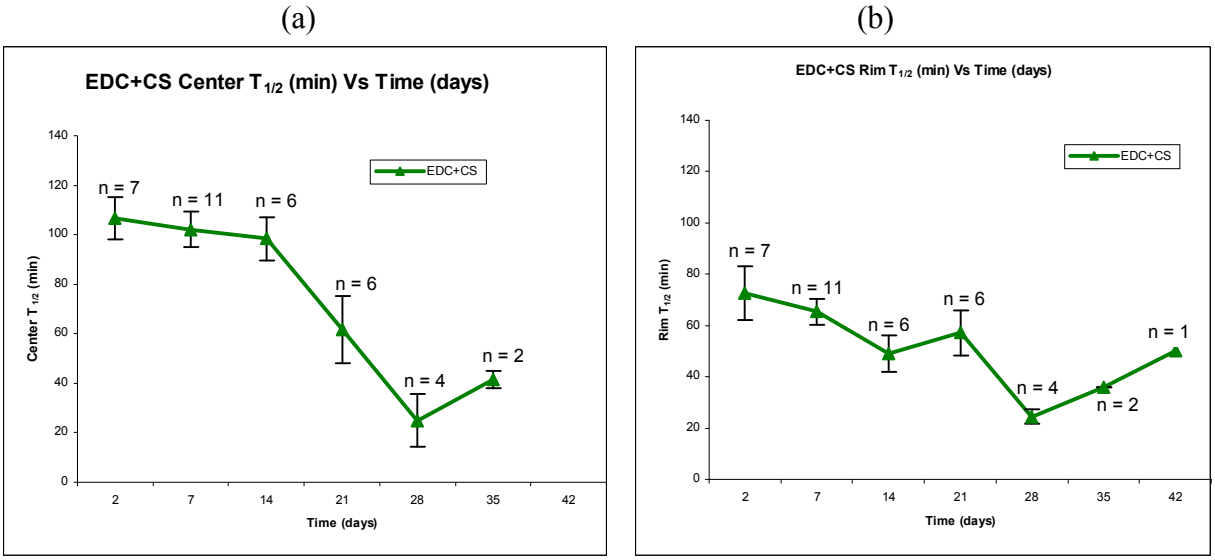

Figure 4-27. Plots of the Mean $T_{1/2}$-time Values in the Center (a) and Rim (b) ROIs of the EDC+CS Sponges as a Function of Implantation Time (n = number of sponge samples; error bars represent SEM).

Table 4-5. Statistical Results for $T_{1/2}$-Time Values in the Center ROIs of the EDC+CS Sponges as a Function of Implantation Time (n/a: not applicable because of insufficient data due to sponge degradation).

Comparison	Day 7	Day 14	Day 21	Day 28	Day 35	Day 42
p (within EDC+CS) (n = 7 @ Day 2)	1.0 (n = 11)	1.0 (n = 6)	0.1 (n = 6)	0.02 (n = 4)	0.2 (n = 2)	n/a (n = 0)

Longitudinal statistical analysis results of EDC and UnX sponges are given below. No statistical analyses were done after Day 28, because of insufficient data due to biodegradation.

Table 4-6. Statistical Results for Changes in EDC Sponge T_2, ADC, TTP and $T_{1/2}$ Values as a Function of Implantation Time.

Study (n @ Day 2)	Day 7	Day 14	Day 21	Day 28
Volume (n = 14 @ Day 2)	0.009 (n = 14)	1.0 (n = 12)	2.8E-06 (n = 8)	1.4E-09 (n = 4)
T_2 (n = 16 @ Day 2)	0.2 (n = 14)	9.3E-08 (n = 12)	1.4E-09 (n = 8)	4.2E-09 (n = 4)
ADC (n = 12 @ Day 2)	0.3 (n = 14)	0.003 (n = 12)	1.3E-05 (n = 7)	0.3 (n = 3)
Time-To-Peak (n = 7 @ Day 2)	0.03 (n = 11)	0.3 (n = 6)	0.001 (n = 4)	0.002 (n = 2)
$T_{1/2}$ (n = 7 @ Day 2)	0.007 (n = 11)	1.0 (n = 6)	0.1 (n = 4)	0.03 (n = 2)

Table 4-7. Statistical Results for Changes in UnX Sponge T_2, ADC, TTP and $T_{1/2}$ Values as a Function of Implantation Time (n/a: not applicable because of insufficient data due to sponge degradation).

Study (n @ Day 2)	Day 7	Day 14	Day 21	Day 28
Volume (n = 14 @ Day 2)	7.8E-01 (n = 14)	8.7E-07 (n = 12)	9.3E-12 (n = 4)	n/a (n = 0)
T_2 (n = 16 @ Day 2)	0.02 (n = 14)	5.7E-09 (n = 12)	7.1E-06 (n = 4)	n/a (n = 0)
ADC (n = 12 @ Day 2)	1.6E-04 (n = 14)	2.E-06 (n = 12)	1.0 (n = 2)	n/a (n = 0)
Time-To-Peak (n = 7 @ Day 2)	1.0 (n = 11)	1.0 (n = 6)	0.001 (n = 2)	n/a (n = 0)
$T_{1/2}$ (n = 7 @ Day 2)	0.008 (n = 11)	0.4 (n = 6)	0.002 (n = 2)	n/a (n = 0)

4.6 Volume Changes as a Function of Implantation Time for Different Sponge Types

Figure 4-28 shows the volume changes for the three types of collagen sponges as a function of implantation time. There was an increase in volume at Day 7 for EDC and EDC+CS sponges, which then started to decrease after Day 14. Complete biodegradation occurred after 21 days for UnX sponges, 35 days for EDC cross-linked sponges, and 42 days for EDC+CS cross-linked sponges. The statistical analysis showed that there was a significant difference between UnX sponges and cross-linked sponges in all time points. The detailed results of the statistical tests, where the data from each sponge are compared with the other two types of sponges at same time points, are summarized in Table 4-8. No statistical analyses were performed for Day 35 and Day 42, because of an insufficient number of sponges. The number sponges compared in each of the analyses are given as n1/n2.

Table 4-8. Statistical Result for Changes in Sponge Volume, for Different Sponge Types, as a Function of Implantation Time (n/a: not applicable because of insufficient data due to sponge degradation).

Comparison	Day 2	Day 7	Day 14	Day 21	Day 28
p (EDC(n1)-EDC+CS(n2))	0.07 (14/14)	0.35 (14/14)	0.1 (12/12)	1.0 (8/8)	1.0 (4/6)
p (EDC(n1)–UNX(n2))	3.5E-05 (14/14)	6.9E-06 (14/14)	1.5E-10 (12/12)	1.8E-02 (8/4)	n/a
p (EDC+CS(n1)–UNX(n2))	6.3E-04 (14/14)	6.8E-07 (14/14)	1.5E-05 (12/12)	1.3E-03 (8/4)	n/a

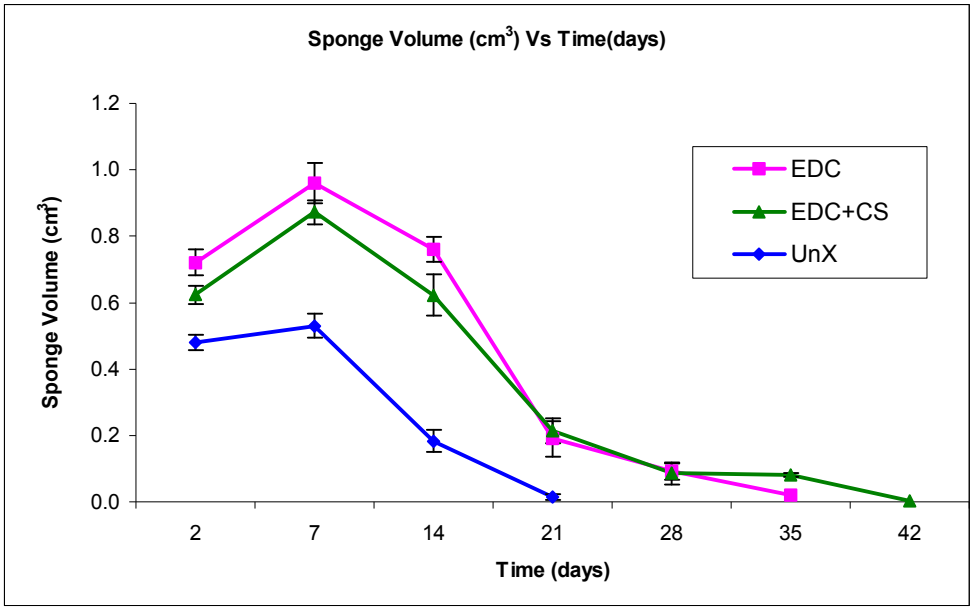

Figure 4-28. Changes in Sponge Volume, for Different Sponge Types, as a Function of Implantation Time (error bars represent SEM).

4.7 Changes in T_2-Relaxation-Time Values as a Function of Implantation Time for Different Sponge Types

Figure 4-29 shows the T_2 changes for the three types of collagen sponges as a function of implantation time. For all sponge types, T_2 values showed a decreasing trend after implantation, but a slight increase was observed after Day 28 for the EDC and EDC+CS sponges. There was a significant difference between UnX and both cross-linked sponges at all time points ($p < 0.01$), except at Day 21. After 28 days, there was a significant difference between EDC and EDC+CS scaffolds ($p < 0.005$). The overall results of the statistical comparisons between the T_2 values for the different sponge types at all time points post-implantation are given in Table 4-9.

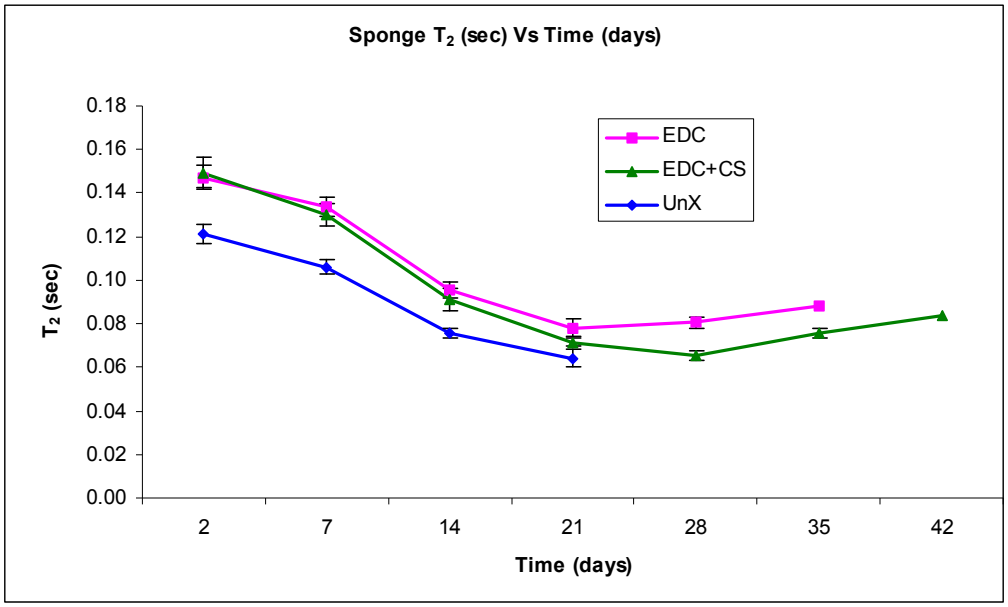

Figure 4-29. Changes T_2-Relaxation-Time Values as a Function of Implantation Time for Different Sponge Types (error bars represent SEM).

Table 4-9. Statistical Result for Changes T_2-Relaxation-Time Values as a Function of Implantation Time for Different Sponge Types (n/a: not applicable because of insufficient data due to sponge degradation).

Comparison	Day 2	Day 7	Day 14	Day 21	Day 28
p (EDC(n1)-EDC+CS(n2))	1.0 (16/16)	0.9 (14/14)	0.8 (12/12)	0.2 (8/8)	0.005 (4/6)
p (EDC(n1)–UNX(n2))	9.2E-04 (16/16)	7.7E-05 (14/14)	6.4E-04 (12/12)	0.06 (8/4)	n/a (4/0)
p (EDC+CS(n1)–UNX(n2))	0.003 (16/16)	7.8E-04 (14/14)	0.03 (12/12)	0.3 (8/4)	n/a (6/0)

4.8 Changes in Short and Long T_2-Relaxation-Time Values as a Function of Implantation Time for Different Sponge Types

Figure 4-30 shows a plot of changes in short and long T_2-relaxation-time values as a function of implantation time for different sponge types. Although the short T_2 values remain relatively constant over time, the long T_2 values decreased at the early time points (< Day 14). The rate of decrease in T_2 values for UnX was faster than both the cross-linked sponges, but all exhibited same trend. After Day 14, it was not possible to distinguish sub-regions within all three

types of sponges as having either long- and short-T_2 values. After Day 14, all sponges appeared to be homogeneous with respect to T_2.

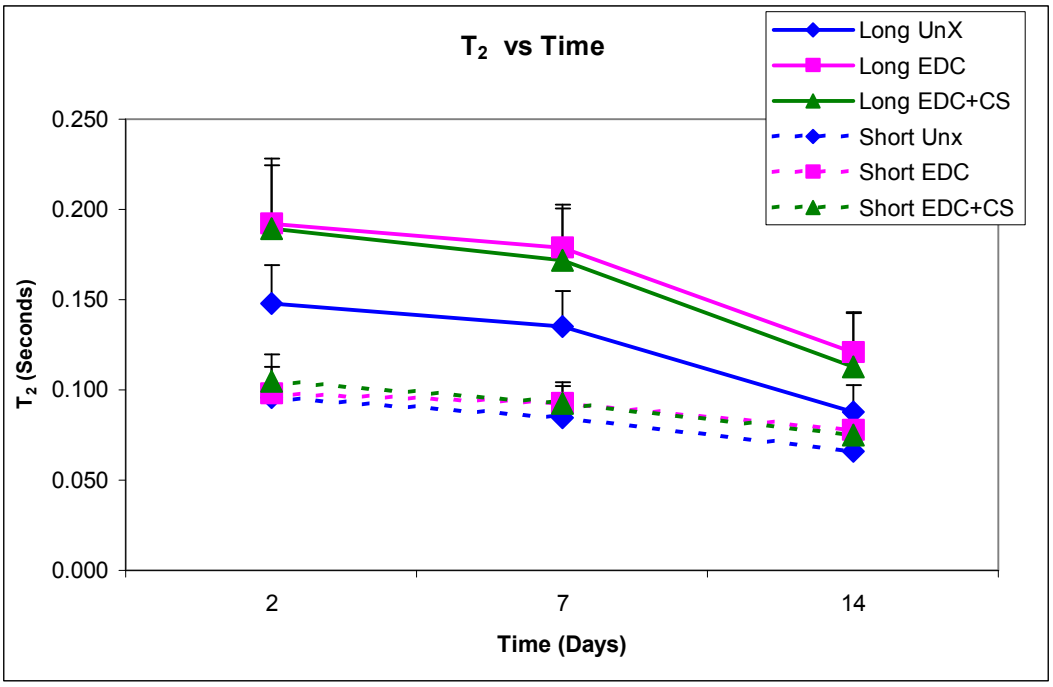

Figure 4-30. Plot of Changes in Short and Long T_2-Relaxation-Time Values as a Function of Implantation Time for Different Sponge Types (error bars represent SEM).

4.9 Changes in Water Apparent Diffusion Coefficient (ADC) Values as a Function of Implantation Time for Different Sponge Types

Figure 4-31 shows a plot of changes in water ADC values as a function of implantation time for different sponge types. All scaffolds showed a decrease in water ADC after implantation. After Day 21, there was no further significant decrease in ADC values for the remaining cross-linked sponges. There was significant difference between EDC and EDC+CS at Day 21 ($p < 0.007$). UnX ADC values were significantly reduced as compared to those of the EDC sponges at all early time points (< 21 days) ($p < 0.03$). EDC+CS and UnX showed similar values at all time points other than at Day 7. Table 4-10 gives the overall statistical results for

changes in water ADC values as a function of implantation time for the different sponge types. The number sponges compared in each of the analyses are given as n1/n2.

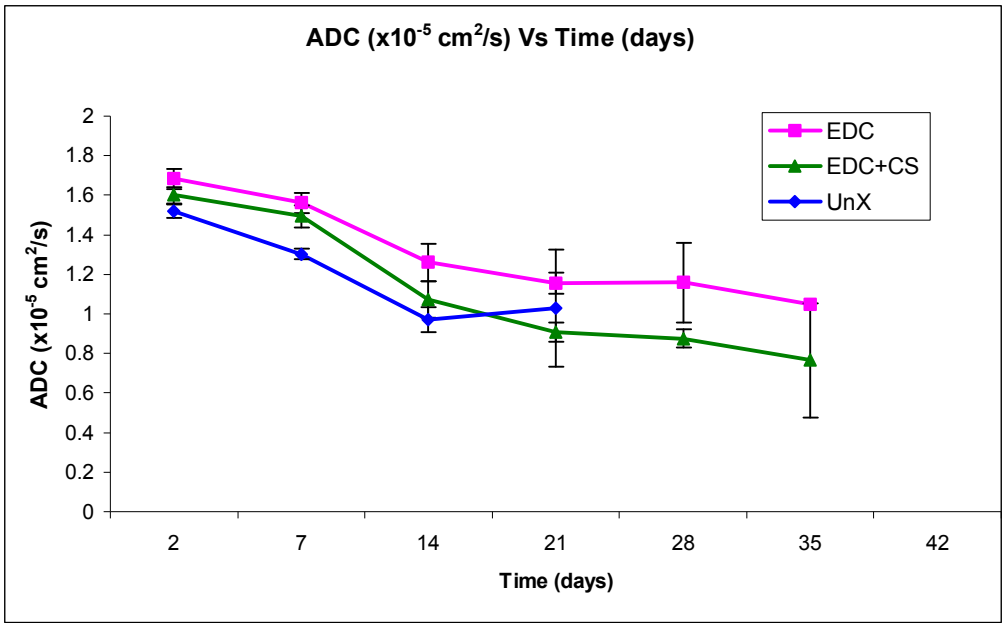

Figure 4-31. Plot of Changes in Water Apparent Diffusion Coefficient (ADC) Values as a Function of Implantation Time for Different Sponge Types (error bars represent SEM).

Table 4-10. Statistical Results for Changes in Water Apparent Diffusion Coefficient (ADC) Values as a Function of Implantation Time for Different Sponge Types (n/a: not applicable because of insufficient data due to sponge degradation).

Comparison	Day 2	Day 7	Day 14	Day 21	Day 28
p (EDC(n1)-EDC+CS(n2))	0.3 (14/14)	0.6 (14/14)	0.3 (12/12)	0.007 (7/8)	0.4 (3/5)
p (EDC(n1)–UNX(n2))	0.02 (14/14)	3.6E-04 (14/14)	0.03 (12/12)	1.0 (7/2)	n/a (3/0)
p (EDC+CS(n1)–UNX(n2))	0.2 (14/14)	9.3E-03 (14/14)	0.5 (12/12)	1.0 (8/2)	n/a (5/0)

4.10 Changes in Time-To-Peak (TTP) Values as a Function of Implantation Time for Different Sponge Types

Figure 4-32 (a) and (b) show plots of changes in TTP values as a function of implantation time for different sponge types. The TTP values showed a decreasing trend in the centers of all three types of sponges. The TTP curve over time for EDC and EDC+CS sponges exhibited the

same trend and comparable values. There was a significant difference between the TTP values of UnX and cross-linked sponges at 2, 14 and 21 Days. The rim region of all three scaffolds showed no significant changes in TTP over time and the rim TTP values for all three sponges were statistically similar at all time points. The overall statistical results for the changes in TTP values as a function of implantation time for the three sponge types are shown in Table 4-11. The number sponges compared in each of the analyses are given as n1/n2.

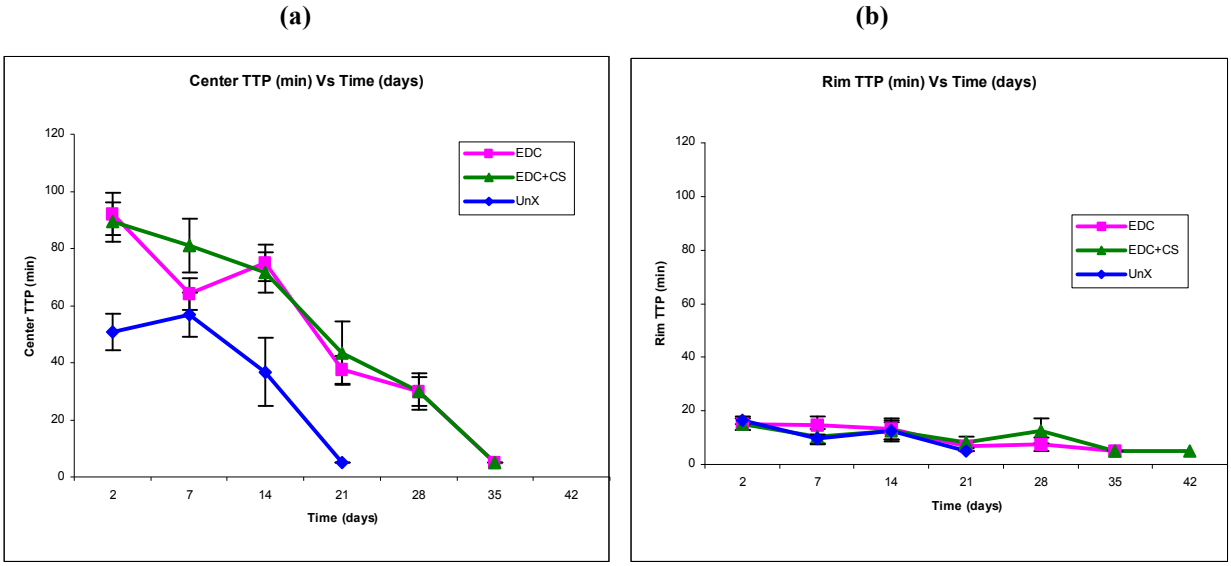

Figure 4-32. Plots of Time-To-Peak (TTP) Values as a Function of Implantation Time in the Center (a) and Rim (b) Regions of Different Sponge Types (error bars represent SEM).

Table 4-11. Statistical Results for Changes in Time-To-Peak (TTP) Values as a Function of Implantation Time for Different Sponge Types (n/a: not applicable because of insufficient data due to sponge degradation).

Comparison	Day 2	Day 7	Day 14	Day 21	Day 28
p (EDC(n1)-EDC+CS(n2))	1.0 (7/7)	0.2 (11/11)	1.0 (6/6)	1.0 (4/6)	1.0 (2/4)
p (EDC(n1)–UNX(n2))	0.002 (7/7)	0.7 (11/11)	0.03 (6/6)	0.01 (4/2)	n/a (2/0)
p (EDC+CS(n1)–UNX(n2))	0.002 (7/7)	0.09 (11/11)	0.05 (6/6)	0.03 (6/2)	n/a (4/0)

4.11 Changes in $T_{1/2}$-Time Values as a Function of Implantation Time for Different Sponge Types

Figure 4-33 (a) and (b) show plots of changes in $T_{1/2}$-time values as a function of implantation time for different sponge types. Similar results were observed for all three sponge types at all time points except Day 7, where the $T_{1/2}$ time of the UnX sponges was significantly reduced as compared to both cross-linked sponges ($p < 0.02$). Similar to the TTP values, no significant changes in $T_{1/2}$-time values were observed in the rim region of any of the sponges. The overall statistical results for changes in $T_{1/2}$-time values in the sponge centers are shown in Table 4-12. Same number of samples was used for both the TTP and $T_{1/2}$-time analyses. The Mason trichrome histological images (Figure 4-34) obtained at Day 28 showed differences in the degree of vascular development between EDC and EDC+CS sponges. However, the contrast-enhanced MRI studies showed the same results for EDC and EDC+CS at all time points.

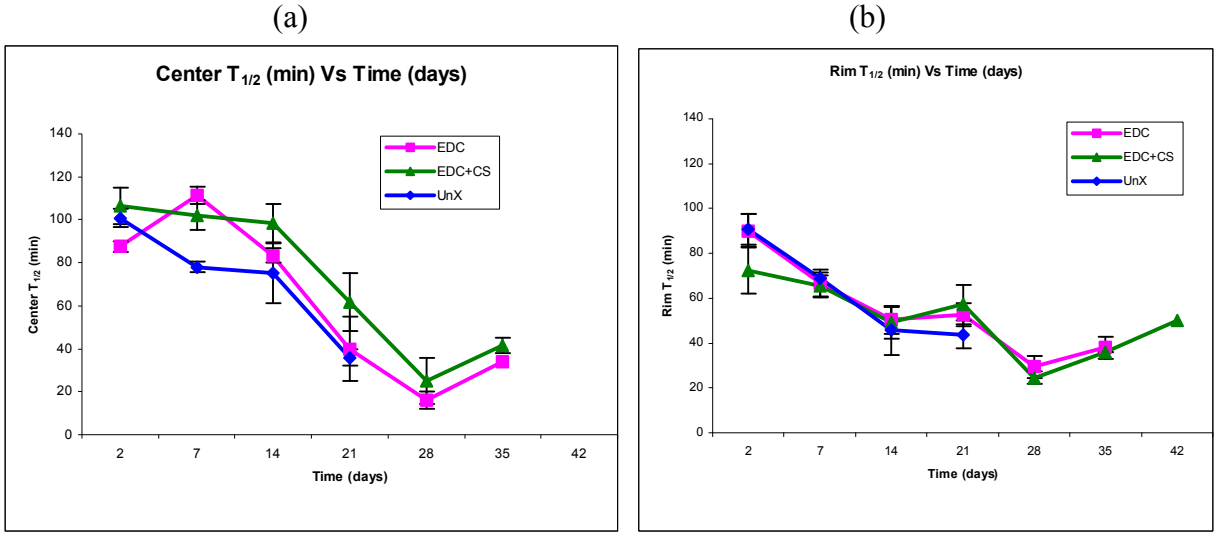

Figure 4-33 Plots of $T_{1/2}$-Time Values as a Function of Implantation Time in the Center (a) and Rim (b) Regions of Different Sponge Types (error bars represent SEM).

Table 4-12. Statistical Results for Changes $T_{1/2}$-Time Values as a Function of Implantation Time in the Center Regions of Different Sponge Types (n/a: not applicable because of insufficient data due to sponge degradation).

Comparison	Day 2	Day 7	Day 14	Day 21	Day 28
p (EDC(n1)-EDC+CS(n2))	0.4 (7/7)	0.4 (11/11)	0.3 (6/6)	0.5 (4/6)	0.7 (2/4)
p (EDC(n1)–UNX(n2))	0.07 (7/7)	3.2E-05 (11/11)	0.9 (6/6)	1.0 (4/2)	n/a (2/0)
p (EDC+CS(n1)–UNX(n2))	0.9 (7/7)	0.02 (11/11)	0.3 (6/6)	0.2 (6/2)	n/a (4/0)

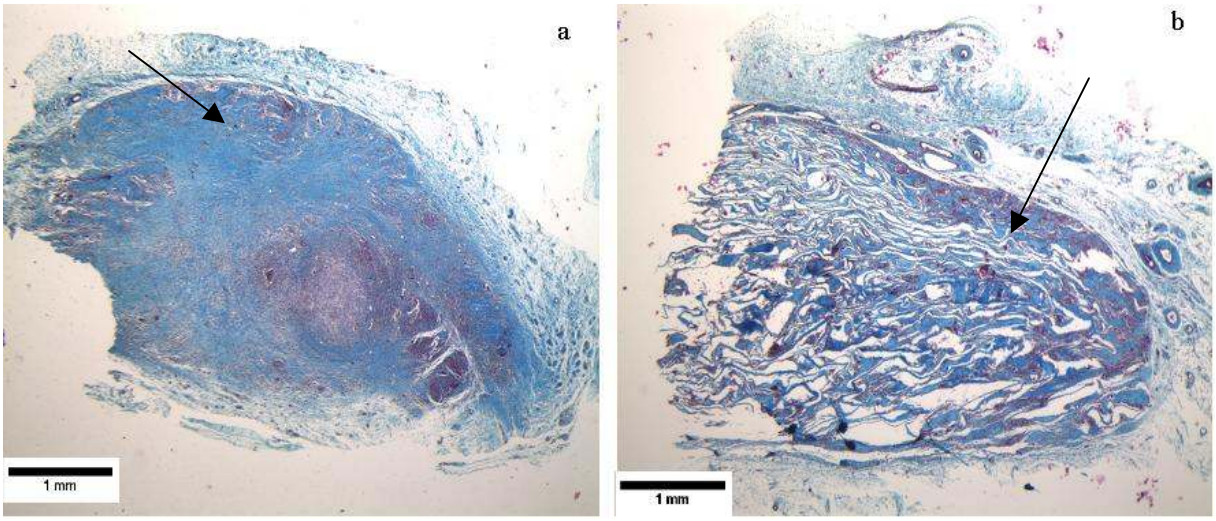

Figure 4-34. Mason Trichrome Histological Images of Day 28 Sponges (a. EDC+CS, b. EDC) (Black dots noted by arrows represent blood vessels)**.**

5 Discussion

5.1 Remodeling of EDC+CS Collagen Sponges over Time Post-Implantation

Within 48 hours after implantation, all the fluids (phosphate buffered saline) in the EDC+CS collagen sponges appeared to be replaced by body fluids. Pieper *et al.* [56] found macrophages were present in low numbers in the implant rims of EDC+CS sponges at Day 2. MRI and histological images both showed a thin layer of cellular infiltration in the sponge rim. The EDC+CS sponges have been shown to have a lamellar-matrix structure and large interstitial spaces at Day 2 [77] and thus capable of storing bulk water. Presumably, this bulk water phase is responsible for the homogeneous appearance of the T_2 and ADC maps as well as the elevated values for both of these parameters.

Figure 5-1 (a) shows the situation that is thought to exist within the sponges at Day 2. There was less integration between the sponges and the surrounding tissue, hence little or no angiogenesis is expected at this time point. Since the biological remodeling of the sponges is very minimal at Day 2, this time point was chosen as a reference point or control for studying the remodeling process.

At Day 7, the inflammatory response of the tissue appears to take place because of the presence of the foreign implant and surgical wound [78]. The wound-healing process initiates a inflammation response, which is characterized by the presence of large number of inflammatory cells, such as macrophages [79]. The inflammatory response resulted in more fluid accumulation inside the sponges, which is thought to be responsible for the nearly 30% increase in sponge volume at that time point. The cells appeared to have infiltrated deeper into the sponge at this time point and formed a thick rim accompanied by the initial onset of angiogenesis [56]. The EDC+CS sponges maintained their lamellar structure and porous structure in the center regions

of the scaffold. The presence of inflammatory cells in the sponge rim are thought to be responsible for the reduced T_2 and ADC values in that region as compared Day 2 (Figure 5-1 (b)).

At Day 14, the overall scaffold volume started decreasing due to biodegradation and resorption of inflammatory fluid [14]. A thin capsule appeared to form around the sponges [56] in an attempt to prevent the direct contact of the sponge with the surrounding tissue [68]. Because of capsule formation and reduced angiogenesis in rim, no significant changes in MRI contrast-agent uptake or washout were observed at this time point. Cellular infiltration has been shown to appeared near the center of the scaffold [56] at this time point and the central volume of the sponge is reduced with an increasingly larger volume of rim (Figure 5-1(c)). Reductions in the water T_2 and ADC values at the sponge center are presumably due to cells infiltrating into the region. The whole-sponge water T_2 and ADC values were also moderately reduced because of the increase in rim volume with increasing tissue ingrowth [14].

At Day 21, cellular infiltration has been observed throughout the scaffold for these sponge types with no apparent "central" region of the sponge visible [68]. The interstitial space in this region is filled with extracellular matrix components and the sponge rims contain larger and fewer giant cells. Because of the cellular concentration gradient through the sponge, the ADC values showed significant contrast between rim and center. By contrast, the T_2 values were homogeneous throughout the sponge at this time point. A significant decrease in sponge volume (nearly 60%) was observed at Day 21, presumably due to remodeling and biodegradation.

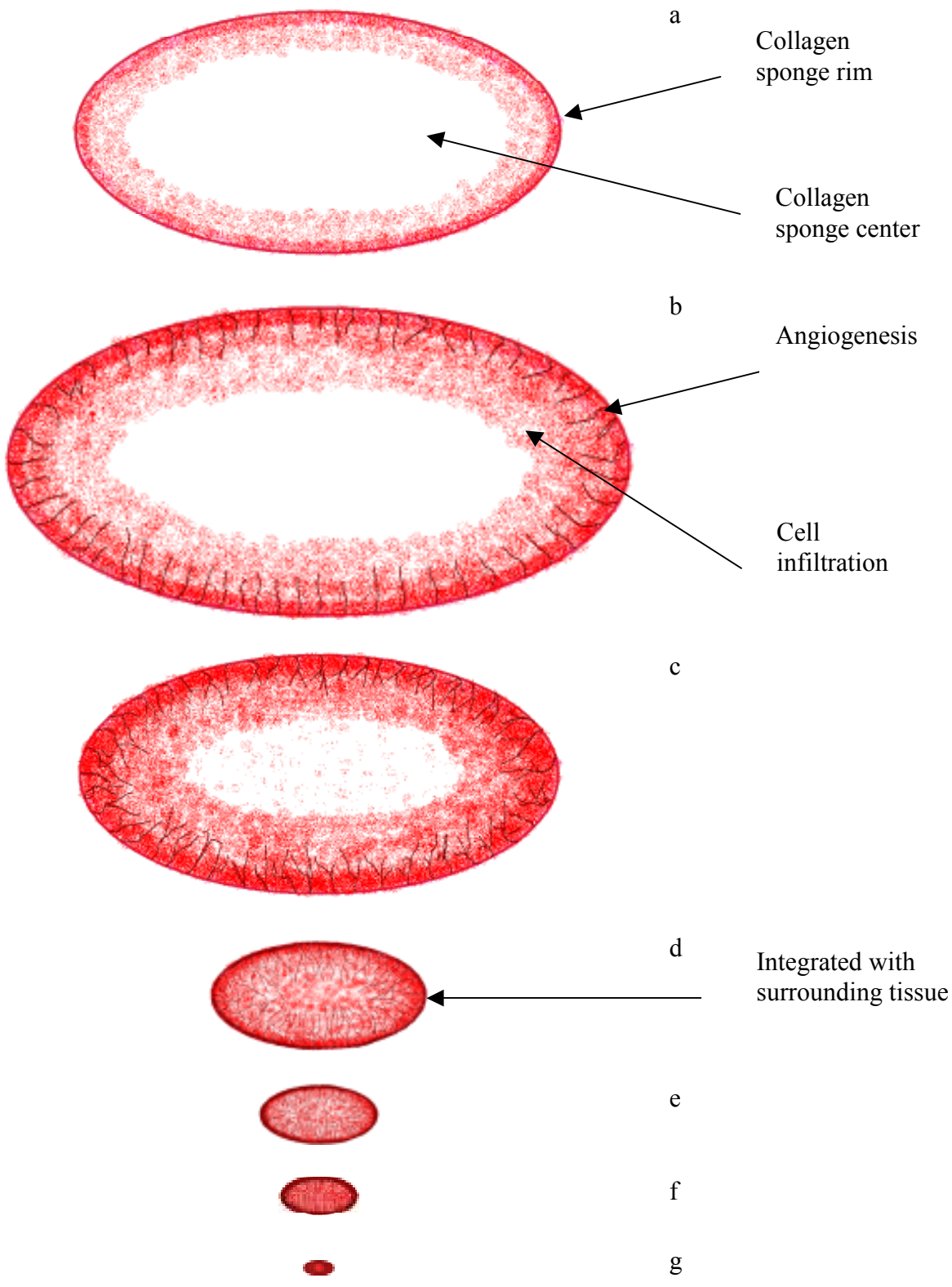

Figure 5-1. Model for Collagen Sponge Remodeling in the Current Study (a. Day 2, b. Day 7, c. Day 14, d. Day 21, e. Day 28, f. Day 35, g. Day 42).

Previous studies using these sponge types have shown that a thick layer of capsule forms around the scaffold and blood vessels are established inside the scaffold [77] (Figure 5-1(d)). Due to angiogenesis as well as a reduction in the thickness of the sponges, the time required for the MRI contrast agent to reach the center of the sponge was reduced. This resulted in shorter Time-To-Peak and $T_{1/2}$-time values for the time points after Day 21.

At Day 28, no porous or lamellar matrix structures were found in the sponges. Qualitative analysis of the histological sections revealed homogenous and complete cellular infiltration at this time point, consistent with observations from earlier studies [68]. The sponges were well-integrated with the surrounding tissues. Cellular infiltration and angiogenesis were well established and the scaffolds were well-integrated with the surrounding tissue (Figure 5-1 (e)). These types of sponges have been shown to be compressed after 28 days [56], which, in conjunction with angiogenesis, could explain the reduced contrast agent uptake and washout times at this time point.

At Day 35, most of scaffolds were biodegraded. The small amount of remaining collagen scaffold was covered with tissue fascia (Figure 5-1 (f)). The contrast-enhanced MRI studies showed that the uptake and washout times in the sponge center were similar to those in the rim region of the sponge. After Day 28, there were no other apparent changes in physiological conditions of the sponge, other than a reduction in volume.

At Day 42, a very small volume of collagen scaffold remained surrounded by a small volume of capsule (Figure 5-1 (g)). From Day 2, the water T_2 and ADC values decreased steadily until they coincided with those of the surrounding tissues [14] and thus are good indicators of the remodeling process.

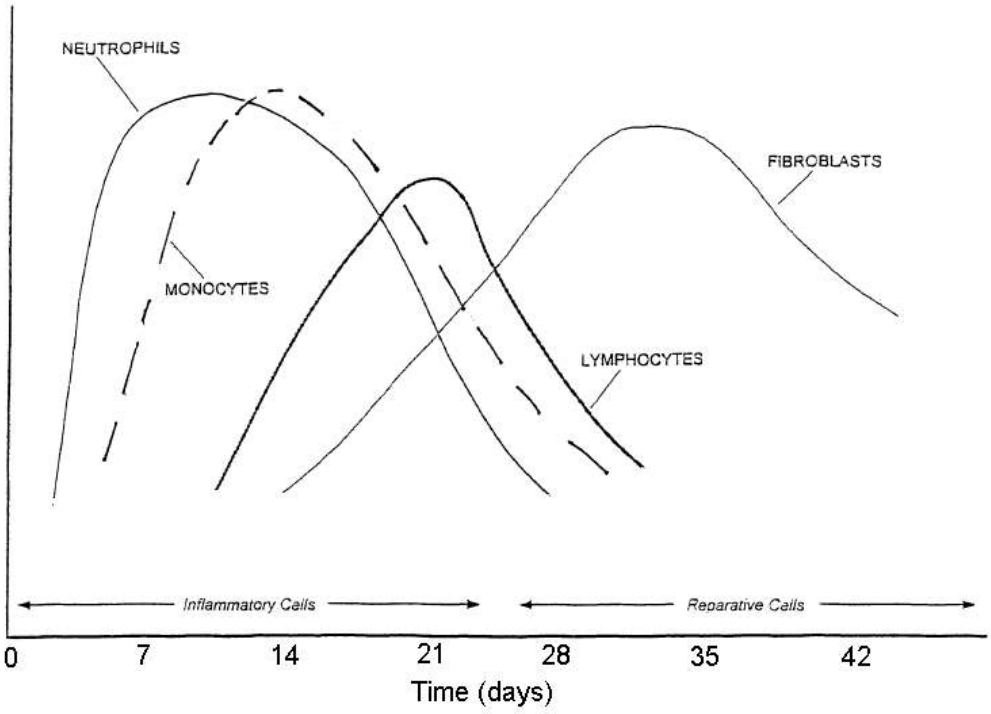

Figure 5-2. Adapted Schematic Representation of Various Cell Population Present During the Wound Healing Process [49].

The increased fluid accumulation at Day 7, responsible for the ~30% increase in sponge volume, did not appear to increase the water T_2 and ADC values. This is presumably because the biofluid composition had not changed significantly as compared to Day 2 [77]. After Day 21, as shown in Figure 5-2, the replacement of inflammatory cells with fibroblasts reduces the bulk water content and hence T_2 to a relatively constant value after 21 days [49].

It appears that changes in the calculated water T_2 and ADC maps are consistent with an increase in cellular infiltration and cell density; processes that reflect the *in vivo* remodeling of the collagen sponges. Consequently, the rate of remodeling of collagen sponges *in vivo* can be evaluated non-invasively by monitoring the progressive changes in MR images and MR tissue parameters over time. The rate of volume change over time post-implantation can be assessed by T_2-weighted images and the rate of cell infiltration changes over time can be monitored using both calculated water T_2 and ADC maps.

The contrast-enhanced studies showed a significant reduction in contrast-agent uptake and washout times after Day 14, which was consistent with angiogenesis formation after Day 14 in implanted scaffolds [77] and connective tissue integration with sponges [68]. Since the sponge rim regions were always in close proximity to the vasculature, little difference was observed in the contrast-agent uptake and washout times over the course of the studies. Nevertheless, the results from the contrast-enhanced studies were consistent with tissue ingrowth and angiogenic development over time in the implanted collagen sponges.

5.2 Volume Changes as a Function of Implantation Time for Different Sponge Types

The UnX scaffold volume decreased faster than either of the cross-linked sponges, presumably because of its lower resistance to biodegradation. Within 24 hours, UnX sponges are known to induce intense tissue reactions, because of their higher antigenicity when compared to the other two sponge types [57]. This is expected because cross-linking is known to increase resistance to biodegradation and enhance biocompatibility [53]. It is assumed that volume changes reflect the extent of biodegradation of the sponge [49]. EDC+CS scaffolds persisted longer than EDC sponges, presumably because of the increased biocompatibility provided by the presence of chondroitin sulfate, which reduced the foreign body reactions. This is because glycosaminoglycans and chondroitin sulfate regulate the inflammatory processes by binding and modulating the growth factors and cytokines, in addition to their immunosuppressive properties [56]. The differential rate of volume change, between uncross-linked and cross-linked sponges ($p < 0.0001$), was clearly apparent in the T_2 maps and thus this MRI parameter is well-correlated with processes associated with collagen sponge remodeling.

5.3 Cell Infiltration as a Function of Implantation Time for Different Sponge Types

The T_2 values, which reflect tissue in-growth and cellular infiltration, decreased significantly from Day 2 in UnX sponges as compared to cross-linked sponges ($p < 0.03$). At the early points, this is presumably due to the more intense tissue response induced by UnX sponges relative to their cross-linked counterparts [57]. Polymorphonuclear cells (PMNs) are known to infiltrate the rim region of such implants rim after 2 days, which may be responsible for the thin dark rim in the water T_2 and ADC maps at Day 2. The EDC+CS sponges are known to exhibit increased cellular infiltration when compared to EDC sponges [77]. This results in filling the scaffold pores with cells such as macrophages, fibroblasts, and extracellular matrix components. This is expected to reduce the bulk water volume and thus shorten the T_2 relaxation time. This may explain why the EDC+CS sponges showed slightly lower T_2 and ADC values at the early time points as compared to the EDC sponges. Since the cross-linked sponges are mechanically stiffer, they are better able to maintain their pore structures (and thus bulk water content) within the subcutaneous pockets at the early time points. As a result, the water T_2 and ADC values would be expected to be significantly higher for the EDC and EDC+CS sponges as compared to the UnX sponges; consistent with our results.

After 28 days, the difference in T_2 and ADC values between EDC and EDC+CS sponges can be attributed to greater tissue in-growth in the EDC+CS as confirmed by previous histological studies [77]. This result is consistent with the literature that shows greater biocompatibility and better tissue integration when chondroitin sulfate is used [56]. This confirms that water T_2 and ADC maps are sensitive to the rate of cellular infiltration and tissue ingrowth in collagen sponges.

5.4 Changes in MRI Contrast Agent Uptake and Washout at a Function of Implantation Time for Different Sponge Types

The reduced time to attain the peak signal-intensity value in the center of the sponges after Day 14 in UnX, and after Day 21 in cross-linked sponges, is attributed to angiogenesis [75]. A greater number of blood vessels within the scaffold increase the delivery of the MRI contrast agent, which diffuses from the blood into the surrounding tissue [21]. Due to the greater thickness of cross-linked scaffolds compared with UnX, the MRI contrast agent has further to diffuse from the rim, where the majority of the blood supply is located, to the center of the scaffold where the measurements were taken.

UnX sponges exhibited reduced TTP values as compared to the cross-linked sponges at the same time point and attained the minimum TTP value at earlier points (< 21 days) in the time course as compared to the cross-linked sponges. This is presumably because of its induced reaction with tissue, increased vascularization, and reduced thickness [57]. The contrast-agent uptake and washout times were significantly different between UnX and cross-linked sponges at the early time points, when the rate of angiogenic formation was different between the sponge types because of biocompatibility.

There was a significant difference in TTP values at Day 2 and Day 14 ($p < 0.05$), and in $T_{1/2}$-time values at Day 7 ($p < 0.02$), between UnX and cross-linked sponges. These results suggest that the effects of resistance to biodegradation and enhanced biocompatibility on angiogenic formation can be investigated using MRI contrast agent studies.

5.5 Limitations

The MRI studies were not able to differentiate between infected sponges, where there was a significant accumulation of pus, and non-infected normal scaffolds. In this case, the higher levels of cellular debris had a similar effect in reducing water T_2 and ADC values as compared to increased cellular infiltration.

To ensure the sponges are large enough to identify them in MR images, it was necessary to make them thicker than usual. This may have resulted in greater heterogeneity within the sponge pore structure, which is not desirable for MRI measurements and analysis.

6 Conclusions and Future Studies

6.1 Conclusions

MRI has successfully been used to non-invasively monitor the biological remodeling of collagen scaffolds *in vivo*. This study has laid the groundwork to further develop of this methodology for additional pre-clinical applications and eventual clinical use.

Water T_2, water ADC and MRI contrast agent uptake and washout profiles have been shown to be sensitive to temporal changes within the collagen sponges in response to biological remodeling. The effects of collagen sponge properties – such as resistance to biodegradation and enhanced biocompatibility – on biodegradation, tissue ingrowth/cellularity and angiogenesis can be effectively studied using this MRI methodology. T_2-weighted MR imaging can be used to evaluate sponge-volume changes over time. Boundaries between normal tissue, fibrous capsule and the sponge were easily distinguished using T_2-weighted MRI. Changes in T_2 relaxation times provided information about the cellularity of the scaffold. Increased cellularity was generally associated with shorter T_2 relaxation times.

Diffusion-weighted MR imaging (DWI) and calculated water ADC values also exhibited changes associated with biological remodeling. However, these changes were not as large as those observed for T_2 or were the trends as clear as those obtained from the T_2 studies. This may in part be due to the lower-spatial-resolution (~1000 microns/pixel) imaging which was used to acquire the ADC data. Diffusion-weighted MRI was shown to be useful for distinguishing the boundary between the formed capsule and the sponge.

Results from the contrast-enhanced MR imaging studies were consistent with changes in vascularity as a function of implantation time. The reduced time-to-peak and $T_{1/2}$-time values

suggested an increasing number of blood vessels infiltrating the scaffold. Contrast-enhanced MR imaging also was able to differentiate the scaffold from the surrounding tissues.

6.2 Future Studies

Extending the study with more samples and more animals would improve the power of the statistical analysis (with a minimum of 4 sponges/time point) at the later time points (> 35 days). Using higher resolution images would help more accurate information to be acquired; improving the identification of trends that may be less clear, such as cellular infiltration, tissue ingrowth and capsule boundaries.

New biomaterials that have longer residence times *in vivo* may help to acquire long-term data, which may further the development of this non-invasive monitoring method. One of the drawbacks of collagen is that it is quickly remodeled and integrated with the host tissue. Another important consideration is to ensure that these scaffolds are sterile and remain sterile during implantation, in order to avoid infection, which could not be distinguished from the normal biological remodeling process using MR images. Making uniform, more homogenous scaffolds would also reduce the statistical variability in the study.

K-means clustering techniques could be applied in the MRI analysis to further classify the sponge heterogeneity and physiological conditions, which could provide more effective evaluation of the implanted sponges [80].

Culture the sponges *in vitro* with fibroblast cells. MR cell labeling techniques could then be used to monitor the fibroblasts cells, to study and track the transplanted cells and their behavior in the implant over time under different physiological conditions [81].

7. References

1. Dowdey JE, Thomas SC, Murry RC (1990), Physics of diagnostic radiology. 4 ed, Lea & Febiger.
2. Vlaardingerbroek MT, den Boer JA (1999), Magnetic Resonance Imaging: Theory and Practice, Springer-verlag.
3. Morris PG (1986), Nuclear Magnetic Resonance Imaging in Medicine and Biology, Clarendon Press, Oxford, England.
4. Harris RK (1986), Nuclear Magnetic Resonance Spectroscopy: A physicochemical View, Longman Scientific & Technical, Essex, England.
5. Farrar TC, Becker ED (1971), Pulse and Fourier Transform NMR: Introduction to Theory and Methods, Academic Press, Orlando.
6. Gadian DG (1995), Nuclear Magnetic Resonance and Its Applications to Living Systems. 2 ed, Oxford University Press, Oxford, England.
7. Tofts P (2003), Quantitative MRI of the brain : measuring changes caused by disease, Wiley, Hoboken, NJ.
8. King KF, Bernstein MA, A, Zhou XJ (2004), Handbook of MRI pulse sequences, Elsevier Academic Press, Burlington, MA.
9. Salibi N, Brown MA (1998), Clinical MR Spectroscopy: First Principles, Wiley-Liss, Inc, New York.
10. Cameron IL, Fullerton GD (1988), Biomedical Magnetic Resonance Imaging, VCH Publishers, Inc., New York.
11. Marois Y, Alikacem N, Zhang Z, Jakubiec B, Roy R, King MW, Guidoin R (1999), Tissue reactions to polypyrrole-coated polyesters: A magnetic resonance relaxometry study. *Artif Organs* 23(**10**):910-919.
12. Chang DC, Hazlewood CF, Nichols BL (1974), Nuclear magnetic resonance transverse relaxation time of water protons in skeletal muscle. *Biophys J* 14:583-606.
13. Packer KJ (1977), The dynamics of water in heterogeneous systems. *Phil. Trans. R. Soc. Lond* 278:59-87.
14. Woerly S, Traoré AS, Doan VD, Marois Y, Guidoin R (2000), In vivo magnetic resonance imaging and relaxometry study of a porous hydrogel implanted in the trapezius muscle of rabbits. *Tissue Eng* 6(**3**):265-278.
15. Gallaz B, Van Beers BE, Pringot J (1997), Contrast-enhanced MR imaging of the liver. *Radiology* 203:297-306.
16. Zhang H, Prince MR, Dong Q, Ersoy H (2003), A Primer for dynamic MR contrast injection. . *Applied Radiology* October:28-36.
17. Bretthorst LG, Quirk JD, Neil JJ, Ackerman JH (2001), Measurement of transmembrane water exchange rate for the *in situ* rat brain. *Proc. Intl. Soc. Mag. Reson. Med* 9:352.
18. Wood ML, Runge VM, Kaufman D, Price AC (1988), Gd DTPA Future applications with advanced imaging techniques. *RadioGraphics* 8(**1**):161-179.
19. Sotak CH, Wedeking P, Telser J, Kumar K, Chang CA, Tweedle MF (1992), Quantative dependence of MR signal intensity of tissue concentrations of Gd(HP-DO3A) in the nephrectomized rat. *Magn Reson Imaging* 10:97-108.
20. Wielopolski PA, Preda A, ten Hagen TLM, van Vliet M, Veenland JF, Ambagtsheer G, van Tiel ST, Vogel MW, Eggermont AMM, Krestin GP, van Dijke CF (2004), Dynamic contrast-enhanced MRI using macromolecular contrast media for monitoring the

response to isolated limb perfusion in experimental soft-tissue sarcomas. *MAGMA* 17:296-302.
21. Morris IT, Hicks CR, Vijayasekaran S, Fallon MJ, McAllister J, Chirila VT, Clayton AB, Crawford GJ, Constable IJ (1999), Correlation of histological findings with gadolinium enhanced MRI scans during healing of a PHEMA orbital implant in rabbits. *Br J Ophthalmol* 83:616-621.
22. Douglas H, Cynthia M, Paschal B (2004), K-space in the clinic. *J Magn Resonance Imaging* 19:145-159.
23. McKeever PE, Chenevert TL, Ross BD (1997), Monitoring early response of experimental brain tumors to therapy using diffusion Magnetic Resonance Imaging *Clin Cancer Res* 3:1457-1466.
24. Stegman LD, Chenevert TL, Taylor JMG, Robertson PL, Greenberg HS, Rehemtulla A, Ross BD (2000), Diffusion Magnetic Resonance Imaging: an early surrogate marker of therapeutic efficacy in brain tumors. *J Natl Cancer Inst* 92:2029-2036.
25. Muthupillai R, Holder CA, Mukundan S, Eastwood JD, Hudgins PA (2000), Diffusion-weighted MR imaging of the normal human spinal cord *in vivo*. *AJNR Am J Neuroradiol* 21:1799-1806.
26. Westrin BA, Axelsson A (1991), Diffusion in gels containing immobbilized cells: A critical review. *Biotechnol Bioeng* 38:439-446.
27. Haraldseth O, Lyng H, Rofstad EK (2000), Measurement of cell censity and necrotic fraction in human melanoma xenografts by Diffusion Weighted Magnetic Resonance Imaging. *Magn Reson Med* 43:828-836.
28. Hong L, Peptan IA, Xu H, Magin RL (2006), MR assessment of osteogenic differentiation in tissue-tngineered constructs. *Tissue Eng* 12(**4**):843-854.
29. Gore JC, Lepage M (2004), Contrast mechanism in Magnetic Resonance Imaging. *Journal of Physics: Conference Series* 3:78–86.
30. Bosch CS, Ackerman JH (1992), Surface coil spectroscopy. *NMR basic principles and progress* 21:4-44.
31. Evelhoch JL, Ackerman JH (1983), NMR T1 measurements in inhomogeneous B1 with surface coils. *J Magn Resonance* 53:52-64.
32. Grove TH, Ackerman JH, Wong GG, Gadian DG, Radda GK (1980), Mapping of metabolities in whole animals by 31P NMR using surface coils. *Nature* 283:167-170.
33. Langer R, Vacanti J (1993), Tissue Engineering. *Science* 260(**5110**):920-926.
34. Burke JF, Yannas IV, Orgill DP, Skrabut EM (1982), Wound tissue can utilize a polymeric template to synthesize a functional extension of skin. *Science* 215(**4529**):174-176.
35. Paul H, Bell E, Buttle DJ, Nakatsuji T (1981), Living tissue formed in vitro and accepted as skin-equivalent tissue of full thickness. *Science* 211(**4486**):1052-1054.
36. Govignon E, Guerret S, Hartmann DJ, Ronfard V (2003), Long-term remodeling of a bilayered living human skin equivalent (Apligraf) grafted onto nude mice: immunolocalization of human cells and characterization of extracellular matrix. *Wound Repair Regen* 11:35-45.
37. Hong SR, Choi YS, Lee YM, Song KW, Park MH, Nam YS (1999), Study on gelatin-containing artificial skin: I. Preparation and characteristics of novel gelatin-alginate sponge. *Biomaterials* 20:409-417.
38. Integra Life Sciences Inc.

39. Griffith LG (2002), Emerging design principles in biomaterials and scaffolds for Tissue Engineering. *Ann. N.Y. Acad. Sci.* 961:83-95.
40. Sachlos E, Czernuszka JT (2003), Making tissue engineering scaffolds work. *European Cells and Materials* 5:29-40.
41. Weir M, Washburn NR, Anderson P, Potter K (2004), Bone formation in polymeric scaffolds evaluated by proton magnetic resonance microscopy and X-ray microtomography. *J Biomed Mater Res* 69A:738-747.
42. Singla A, Lee CH, Lee Y (2001), Biomedical applications of collagen. *Intl J Pharm* 221:1-22.
43. Apel J, Schoof H, Heschel I, Rau G (2001), Control of Pore Structure and Size in Freeze-Dried Collagen Sponges. *J Biomed Mater Res (Appl Biomater)* 58:352–357.
44. Friess W (1998), Collagen-biomaterial for drug delivery. *Eur J Pharm Biopharm* 45(**2**):113-136.
45. Campbell GR, Thomas AC, Campbell JH (2003), Advances in vascular tissue engineering. *Cardiovasc Pathol* 12(**5**):271-276.
46. Bell E, Weinberg CB (1986), A blood vessel model constructed from collagen and cultural vascular cells. *Science* 231:397-400.
47. Abraham G, Huynh T, Murray J, Brockbank K, Hagen P, Sullivan S (1999), Remodeling of an acellular collagen graft into a physiological responsive neovessel. *Nat Biotechnol* 17:1083-1086.
48. PaQuet S, L'heureux N, Labbe R, Germain L, Auger FOA (1998), A completely biological tissue-engineered human blood vessel. *The FASEB Journal* 12:48-56.
49. Bailey AJ (2000), The fate of collagen implants in tissue defects. *Wound Repair Regen* 8(**1**):5-12.
50. Harley BA, O'Brien FJ, and Yannas IV, Gibson L (2004), Influence of freezing rate on pore structure in freeze-dried collagen-GAG scaffolds. *Biomaterials* 25(**6**):1077-1086.
51. Murray J, Billiar K, Laude D, Abraham G, Bachrach N (2001), Effects of carbodiimide crosslinking conditions on the physical properties of laminated intestinal submucosa. *J Biomed Mater Res* 56:101-108.
52. Hafmans T, Pieper JS, Veerkamp JH, van Kuppevelt TH (2000), Development of tailor-made collagen glycosaminoglycan matrices: EDC/NHS crosslinking, and ultrastructural aspects. *Biomaterials* 21:581-593.
53. Spector M, Pek YS, Yannas IV, Gibson LJ (2004), Degradation of a collagen–chondroitin-6-sulfate matrix by collagenase and by chondroitinase. *Biomaterials* 25:473-482.
54. Yao C, Steffens GCM, Prével P, Markowicz M, Schenck P, Noah EM, Pallua N (2004), Modulation of Angiogenic Potential of Collagen Matrices by Covalent Incorporation of Heparin and Loading with Vascular Endothelial Growth Factor. *Tissue Eng* 10(**9**):1502-1509.
55. Klebe RJ, Kleinman HK, Martin GR (1981), Role of collagenous matrices in the adhesion and growth of cells. *J Cell Biol* 88:473-485.
56. Oosterhof A, Pieper JS, Dijkstra PJ, Veerkamp JH, van Kuppevelt TH (2000), Attachment of glycosaminoglycans to collagenous matrices modulates the tissue response in rats. *Biomaterials* 21(**16**):1689-1699.
57. Plantinga JA, van Wachem PB, Wissink MJB, Beernik R, Poot AA, Engbers GHM, Beugeling T, van Aken WG, Feijen J, van Luyn MJA(2001), *In vivo* biocompatibility of

carbodiimide-crosslinked collagen matrices: Effects of crosslink density, heparin immobilization, and bFGF loading. *J Biomed Mater Res* 55:368-378.
58. Steer DL, Nigam SK(2003), Developmental approaches to kidney tissue engineering. *Am J Physiol Renal Physiol* 286:F1-F7.
59. Bursac N, Papadaki M, Langer R, Merok J, Vunjak-Novakovic G, Freed LE (2001), Tissue engineering of functional cardiac muscle: molecular, structural, and electrophysiological studies. *Am J Physiol Heart Circ Physiol* 280:H168-H178.
60. Lee E, Yannas IV, Orgill DP, Skrabut EM, Murphy GF (1989), Synthesis and characterization of a model extracellular matrix that induces partial regeneration of adult mammalian skin. *Science* 96(**3**):933-937.
61. Kosnik PE, Dennis RG, Gilbert ME, Faulkner JA (2001), Excitability and contractility of skeletal muscle engineered from primary cultures and cell lines. *Am J Physiol Cell Physiol* 280:288-295.
62. Black RA, Seliktar D, Vito RP, Nerem RM (2000), Dynamic mechanical conditioning of collagen-gel blood vessel constructs induces remodeling in vitro. *Ann Biomed Eng* 28:351-362.
63. Gooch KJ, Sieminski AL (2000), Biomaterial-microvasculature interactions. *Biomaterials* 21:2233-2241.
64. Chvapil M (1977), Collagen sponge: theory and practice of medical applications. *J Biomed Mater Res* 11(**5**):721-741.
65. Harley BA, O'Brien FJ, Yannas IV, Gibson L (2005), The effect of pore size on cell adhesion in collagen-GAG scaffolds. *Biomaterials* 26:433-441.
66. Khor E (1997), Methods for the treatment of collagenous tissues for bioprostheses. *Biomaterials* 18(**2**):95-105.
67. Lee JM, Gratzer PF (2001), Control of pH alters the type of cross-linking produced by 1-ethyl-3-(3-dimethylaminopropyl)-carbodiimide (EDC) treatment of acellular matrix vascular grafts. *J Biomed Mater Res* 58(**2**):172-179.
68. Viljanto J, Martson M, Laippala P, Saukko P (1999), Cranio-caudal differences in granulation tissue formation: an experimental study in the rat. *Wound Repair Regen* 7:119-126.
69. Hedlund LW, Qiu HH, Neuman MR, Edwards CR, Black RD, Cofer GP, Johnson AG (1998), Measuring the progression of foreign body reaction to silicone implants using in vivo MR Microscopy. *IEEE Transactions on biomedical engineering* 45(**7**):921-927
70. Moses MA, Rickert D, Lendlein A, Kelch S, Franke RP (2003), The importance of angiogenesis in the interaction between polymeric biomaterials and surrounding tissue. *Clin Hemorheol Microcirc* 28:175-181.
71. Long R, Constantinidis I, Weber C, Safley S, Sambanis A (2001), Non-Invasive monitoring of a bioartificial pancreas in Vitro and in Vivo. *Annals New York Academy Of Sciences* 944:83-95.
72. Oosterhof A, Pieper JS, Dijikstra PJ, Veerkamp JH, van Kuppevelt TH (1999), Preparation and characterization of porous crosslinked collagenous matrices containing bioavailable chodroitin sulphate. *Biomaterials* 20:847-858.
73. Dugas JP, Garbow JR, Song S, Conradi MS (2004), A simple, robust hardware device for passive or active respiratory gating in MRI and MRS experiments. *Magn Reson Eng* 21B:40-48.

74. Bretthorst GL, Quirk JD, Duong TQ, Snyder AZ, Springer CS, Ackerman JH, Neil JJ (2003), Equilibrium water exchange between the intra- and extracellular spaces of mammalian brain. *Magn Reson Med* 50:493-499.
75. Howes SC (2007), Design of a non-invasive system for the evaluation of collagen scaffolds using MRI. *Unpublished data*.
76. Glantz SA (2001), Primier of Biostatistics. 5 ed, McGraw-Hill, New York.
77. Hafmans T, Pieper JS, van Luyn MJA, Brouswer LA, Veerkamp JH, van Kuppevelt TH (2002), Loading of collagen-heparan sulfate matrices with bFGF promotes angiogenesis and tissue generation in rats. *J Biomed Mater Res* 62:185-194.
78. Carmeliet P (2005), Angiogenesis in life, disease and medicine. *Nature* 438:932-936.
79. Mikos A, Patel SZ (2004), Angiogenesis with biomaterial-based drug- and cell-delivery systems. *J. Biomater. Sci. Polymer Edn,* 15(**6**):701-726.
80. Ross AL, Carano RAD, Ross J, Williams SP, Koeppen H, Schwall RH, van Bruggen N (2004), Quantification of tumor tissue populations by multispectral analysis. *Magn Reson Imaging* 51:542-551.
81. Song H, Ko IK, Cho E, Lee ES, Huh Y, Suh J (2007), *In vivo* MR Imaging of Tissue-engineered human mesenchymal stem cells transplanted to mouse: a preliminary study. *Ann Biomed Eng* 35(**1**):101-108.